

The Top Quark at Linear Colliders: Quantum Chromodynamics Corrections

by

Cosmin Macesanu

Submitted in Partial Fulfillment
of the
Requirements for the Degree

Doctor of Philosophy

Supervised by
Professor Lynne H. Orr

Department of Physics and Astronomy
The College
Arts and Sciences

University of Rochester

Rochester, New York

2001

to my family

Curriculum Vitae

The author was born in Bucharest, Romania, on May 13 1973. He attended the Faculty of Physics at the University of Bucharest from 1991 to 1996, and graduated with a Bachelor of Sciences degree in 1996. He came to the University of Rochester in the fall of 1996 and began graduate studies in the Department of Physics and Astronomy. He received a Robert Marshak Fellowship in 1996 and 1997. He pursued his research in the field of elementary particle physics under the direction of Professor Lynne H. Orr and received the Master of Science degree in 1997.

Acknowledgments

First, I want to thank my adviser, Professor Lynne H. Orr, for her support of my work on this thesis and for suggesting the topic in the first place. I would also like to express my gratitude for the cooperation and help of my colleagues and of many postdoctoral fellows who performed research at the University of Rochester these past five years. Among these, I would like to give special thanks to Dr. Doreen Wackeroth, who spend many hours discussing with me the details of the evaluation of the electroweak corrections to the W pair production and decay process, and to Dr. Rob Szalapsky, who helped me with the computation of Passarino-Veltman functions and with the computational details of my work in general. Moreover, I would like to thank Dr. Oleg Yakovlev for a discussion concerning the diagrams contributing to the top production and decay process, and Dr. Alexander Chapovsky for discussions on the DPA approximation and for providing me with routines for the evaluation of nonfactorizable corrections in the soft gluon approximation.

The Top Quark at Linear Colliders: Quantum Chromodynamics Corrections

by

Cosmin Macesanu

Abstract

We present a computation of QCD next-to-leading order corrections to the top production and decay process at linear colliders. The top quarks are allowed to be off-shell and the production and decay subprocesses are treated together, thus allowing for interference effects. We consider the case of real gluon radiation, as well as virtual corrections to the tree level amplitude. The framework employed for our computation is the double pole approximation (DPA). We describe the implementation of this approximation for the top production and decay process and compare it with the implementation of DPA for the evaluation of QED corrections to the W pair production at LEP II. Similarities and differences between the two cases are pointed out.

The theoretical approach we present in this thesis is implemented in a Monte Carlo generator. The total amplitude is separated into gauge invariant parts which can be associated with radiative corrections to production and decay subprocesses, and interference between these. The contributing amplitudes are computed using

spinor techniques, and include all top width effects, spin correlations and b quark mass effects. The results discussed for the real gluon radiation case include studies of the gluon radiation properties and the effects of this radiation on top mass reconstruction. We also examine the effects of interference between production- and decay- stage radiation, whose magnitude is sensitive to the value of the top quark width. After the computation of virtual corrections, we present results for the total top production cross sections, and we analyze the magnitude of nonfactorizable (interference) corrections. We study the impact these corrections can have on the top invariant mass distributions.

Contents

Table of Contents	vii
List of Tables	ix
List of Figures	x
1 Introduction	1
2 Computational Approach	9
2.1 Amplitudes in DPA	9
2.2 Cross sections and infrared singularities	13
2.3 Top width and gauge invariance	17
3 Real gluon radiation	20
3.1 Amplitude evaluation	21
3.1.1 Production–decay decomposition	23
3.1.2 Gauge invariance	25
3.1.3 Monte Carlo and phase space integration	28
3.2 Numerical Results	28
3.2.1 Characteristics of the gluon radiation	29
3.2.2 Mass Reconstruction	33

3.2.3	Interference and Sensitivity to Γ_t	37
4	Virtual corrections	43
4.1	Resonant structure of partial amplitudes	46
4.1.1	Interference diagrams	48
4.1.2	Vertex corrections	51
4.1.3	Renormalization and fermion self-energy	53
4.2	Gauge invariance and corrections to particular subprocesses . . .	55
4.3	Computational Approach	60
4.4	On-shell DPA	63
4.5	Results for virtual corrections and the total cross section	66
5	Conclusions	74
	Bibliography	77
A	Spinor techniques	81
A.1	Spinors describing massive and massless fermions	82
A.2	Spinors describing massless bosons	85
A.3	Spinors describing massive bosons	85
B	Amplitudes and cross sections formulas	87
B.1	Tree level amplitudes	87
B.2	Virtual corrections amplitudes	90
B.3	Cross sections and color factors	93
C	Passarino-Veltman functions	96

List of Tables

4.1	Total cross sections for top production at linear colliders (measured in picobarns), with no cuts on phase space.	68
4.2	Total cross sections for top production at linear colliders (measured in picobarns), with cuts on the top, antitop invariant mass.	69

List of Figures

2-1	The top-antitop diagrams contributing to the process (2.1).	10
2-2	Single top diagrams contributing to the process (2.1).	11
2-3	Feynman diagrams for gluon radiation in top production and decay.	12
2-4	Feynman diagrams for virtual gluon corrections to top production and decay.	14
3-1	The fraction of gluon emissions radiated in the production stage, as a function of minimum gluon energy, for center-of-mass energy 1 TeV (solid line) and 500 GeV (dashed line), with no cuts.	30
3-2	The fraction of gluon emissions radiated in the production stage, as a function of minimum gluon energy, for center-of-mass energy 500 GeV, with no cuts (dashed line), $E_T(g, b) > 3$ GeV (dotted line), and $m_{bg} >$ 10 GeV (solid line).	31
3-3	The spectrum of radiated gluons as a function of gluon energy in GeV for center-of-mass energy 500 GeV, with m_{bg} and m_t cuts (see text). Dashed histogram: production-stage radiation. Dotted histogram: decay-stage radiation. Solid histogram: total.	32
3-4	The top invariant mass spectrum without (left) and with (right) the gluon momentum included, for center-of-mass energy 500 GeV, with m_{bg} cuts and $E_g > 5\text{GeV}$	33

3-5	The distribution in the angle between the gluon and the b quark for center-of-mass energy 500 GeV, with $E_g > 5$ GeV. The various contributions are as described in the text.	34
3-6	The top invariant mass spectrum with b -gluon angle selection criteria (dotted histogram), for center-of-mass energy 500 GeV, minimum gluon energy 5 GeV, and m_{bg} cuts. The solid curve and histogram show the effects of energy smearing.	36
3-7	The distribution in angle between the top quark and the gluon for gluon energies from 5 to 10 GeV, $\cos \theta_{tb}, \cos \theta_{t\bar{b}} < 0.9$, m_t cuts, and 750 GeV collision energy. The upper solid histogram is the total and the other histograms represent the individual contributions: dotted: decay; dashed: production; dot-dashed: decay-decay interference; solid: production-decay interference.	38
3-8	As in Fig. 3-7, with the addition of the cuts given in Eqs. 3.14,3.15. . .	40
3-9	The distribution in angle between the top quark and the gluon for gluon energies from 5 to 10 GeV, $\cos \theta_{tb}, \cos \theta_{t\bar{b}} < 0.9$, and 750 GeV collision energy. The histograms correspond to different values of the top width Γ_t : dot-dashed: 0.1 GeV; solid: 1.42 GeV (SM); dashed: 5. GeV; dotted: 20 GeV.	41
4-1	General vertex correction diagram.	51
4-2	Terms contributing to the renormalized vertex; the dots represent counterterm insertions.	53
4-3	The relative nonfactorizable correction to the invariant mass distribution; the solid line is the contribution of terms proportional to the tree level amplitude, while the dashed line contains also the M_1 terms in Eq. 4.39.	70

4-4	Real gluon interference: the $\sigma_{b\bar{t}}$ term. The solid line corresponds to the semianalytic approach; the dashed line is obtained through numerical evaluation with $M_t = \sqrt{p_{bW}^2}$; the dotted line is obtained through numerical evaluation with M_t given by Eq. 4.48.	71
4-5	The relative nonfactorizable correction to the invariant mass distribution; comparison between the semianalytical (dashed line) and the numerical (solid line) approach.	73

Chapter 1

Introduction

Since ancient times, people have been looking for explanations for the natural phenomena surrounding us. With the birth of the modern scientific method in the 15th - 16th century, great steps forward have been made in our understanding of the natural laws. The body of accumulated knowledge has naturally coalesced into theories which deal with different aspects of reality. Examples of such theories are Newtonian mechanics, which deals with the interaction of normal bodies, optics, which deals with properties of light, and electricity and magnetism, which deals with the electric and magnetic properties of materials. As time has passed, there has been a tendency to look for ways to combine these disparate theories into more fundamental ones, which encompass and explain all the phenomena previously dealt with separately (Maxwell's combination of electricity, magnetism and optics into electromagnetism is such an example). In the past century, these searches have coalesced into a search for a unified theory which underlies all the physical reality around us.

The result is the Standard Model of particle physics. This theory deals with the fundamental constituents of matter and their interactions (except gravity).

According to our present knowledge, all ordinary matter is built from elementary particles: six leptons and six quarks (spin 1/2 particles, or fermions), which are arranged into three families:

$$\begin{array}{ll} \text{Leptons :} & \begin{pmatrix} \nu_e \\ e \end{pmatrix} \quad \begin{pmatrix} \nu_\mu \\ \mu \end{pmatrix} \quad \begin{pmatrix} \nu_\tau \\ \tau \end{pmatrix} \\ \text{Quarks :} & \begin{pmatrix} u \\ d \end{pmatrix} \quad \begin{pmatrix} c \\ s \end{pmatrix} \quad \begin{pmatrix} t \\ b \end{pmatrix} \end{array} \quad (1.1)$$

The interactions of these particles are mediated by the gauge bosons:

$$\text{Gauge bosons : } \gamma, Z_0, W^\pm, g \quad (1.2)$$

which are spin 1 particles. The mathematical framework which describes these interactions is gauge field theory; according to this theory, each generator of the gauge symmetry group of the Lagrangian corresponds to one gauge force carrier. Thus, the photon (γ), Z_0 and W^\pm are carriers of the electroweak gauge force (symmetry group $U(1) \times SU(2)$), which is felt by all particles, while the gluons (g) are the carriers of the strong gauge force (symmetry group $SU(3)$) which mediates the interactions of the quarks among themselves solely.

So far, the successes of the Standard Model are impressive; some of its predictions have been tested with a remarkable degree of accuracy, and, at this time, not a single piece of experimental evidence contradicts it convincingly. Still, there are pieces missing; for example, the exact mechanism of electroweak symmetry breaking (which is responsible for giving masses to the particles in Eqs. 1.1, 1.2) is still unknown. It is surmised that the breaking of electroweak symmetry is driven by yet undiscovered bosons: either the Higgs particle(s), in the most promising models, or maybe top quark condensates (in technicolor models [1]). Supersymmetric (SUSY) models [2], which solve some theoretical problems in the Standard

Model, also predict a whole slew of new particles (supersymmetric partners). In general, there is a great interest today in what lies beyond the Standard Model. (Since it does not include gravity, we know that it cannot be the final theory). It is expected that, in coming years, experiments at higher energies will help answer these questions.

The study of the top quark might shed light on the answer to at least some of these questions. The characteristics of the top quark make it one of the most interesting elementary particles discovered so far. Its mass is quite large, about 175 GeV (we use natural units in which $\hbar = c = 1$); correspondingly, its Yukawa coupling (the coupling to the Higgs boson) is of order unity; and this might be an indication that the top plays a special role in the electroweak symmetry breaking process. Moreover, the top Standard Model width is about 1.5 GeV, thus being much larger than $\Lambda_{QCD} \sim 200$ MeV. This means that the top quark decays before having time to hadronize [3], therefore providing us with a unique opportunity to study the interactions of a bare quark. All these properties, together with the fact that, since the energies involved in the top production and decay processes are large, we can use perturbative QCD for reliable theoretical predictions, insure that the study of the top quark will be one of the main goals of particle physics for the next decade.

The top quark was discovered in 1995 at the Fermilab Tevatron Collider [4]. Only a couple hundreds events have been identified so far. Due to limited statistics, the only precise information available on the top quark so far is its mass ¹; the latest analysis [5] gives the value 174.3 ± 5.1 GeV. The Tevatron Run II, starting this summer, is expected to provide us with a sample of top events about an order of magnitude larger than the one available so far; this will result in more

¹There are also results for other top quark parameters, like the production cross section and its couplings, but the values obtained have large statistical uncertainties.

precise determination of the top mass, width and couplings. The Large Hadron Collider, once it starts operating in 2006, will be a top factory, producing more than 8 million top-antitop pairs annually [6]. However, the analysis of the data coming from hadron colliders is complicated by uncertainties in the initial state, large QCD backgrounds, etc. Thus, even with the large top sample provided by the LHC, the uncertainty in the top mass measurement, for example, will be of order 1 to 2 GeV (due mostly to systematic uncertainties [6]).

An e^+e^- linear collider with center of mass energy greater than the $t\bar{t}$ production threshold (350 GeV) would be an ideal machine for the precision study of the top quark (among other things). At such a collider, the electron and positron in the initial state annihilate and create a top-antitop pair, which in turn each decay into a Wb pair. So far, this machine is in the design stage, with a projected date of completion not before the year 2010. At this time, there are two main designs; the European TESLA and the American-Japanese NLC-JLC (for details about the parameters of these machines, see for example [7]). Both machines are linear accelerators, about 30 Km in length, operating at energies up to 1 TeV (800 GeV for TESLA) with luminosities of order $10^{34} cm^{-2}s^{-1}$ (which means 100 inverse femtobarns per year).

One of the main advantages of an e^+e^- collider versus a hadronic one is that the energy of the initial state is well determined. Thus, it is possible to perform threshold studies for the production of a $t\bar{t}$ pair. The shape of the production cross section near the threshold is quite sensitive to a number of top quark parameters. In this energy range, current analysis indicates that it is possible to measure the top mass with an accuracy of about 40 MeV using only $10 fb^{-1}$ [7]. With a larger data sample, measurements of the top decay width, Yukawa coupling and strong coupling constant at the several percent level can also be achieved. Going to higher energies, we can study the V-A structure of the top quark couplings to the

gauge bosons (γ , Z and W) [8]. The information about couplings can be obtained by using spin correlations: the top quarks are produced in certain spin states, as dictated by the top - γ , Z couplings. Since the top decays before hadronization, the spin states of the top directly influence the angular distributions of its decay products. Simulations show that by analyzing kinematic variables of final state particles we can measure top couplings at the several percent level [7].

Of course, in order to obtain information about fundamental parameters like the top quark mass and couplings, experimental data is only a part of the equation. The other part is a good theoretical understanding of the physical processes which are studied. For the threshold region, comprehensive theoretical studies (NNLO computation with resummation of large logarithms, careful treatment of the renormalon ambiguity) have already been performed [9]. Above threshold, the theory lags behind. At 500 GeV center of mass energy, with a 500 pb^{-1} integrated luminosity, we will get about 3×10^5 top quark pairs created; as a consequence, the experimental accuracy is better than one percent. Ideally, we would like to have a similar (or better) precision in the theoretical predictions.

As for most physical processes, precise theoretical predictions for the top production and decay require the computation of next to leading order corrections (either virtual or real). These can be split into two categories: electroweak corrections, due to the radiation of a photon or weak interaction gauge boson (Z or W), and QCD corrections, due to virtual or real gluon radiation. Since the top is a quark, the QCD corrections are the most important ones, and these corrections will be the subject of the present paper.

First, we start by reviewing previous work done in the area. In the first approximation, the top production and decay processes can be considered separately. The QCD radiative corrections to individual subprocesses have been comprehen-

sively studied. For the top production subprocess:

$$e^+e^- \rightarrow t \bar{t} (g)$$

there are computations for virtual and soft (low energy) gluon radiation [10], as well as for hard (higher energy) gluon radiation ([10], [11], [12], [13] are just some examples). Similarly, the top decay subprocess:

$$t \rightarrow b W (g)$$

has been computed taking into consideration virtual and hard gluons together ([14], [16], [15]).

Using these results, one can try to approximate the top production and decay process by assuming that the intermediate tops are on the mass-shell (narrow width approximation) and treating the subprocesses separately [17]. This assumption is usually reasonable; the result for the total cross section is valid up to terms of order $\Gamma_t/m_t \sim 1\%$. However, finite top width effects, which can be thought of as interference between production and decay subprocesses, can be important in some differential cross sections. Therefore, for precision better than % level, it is necessary to treat the production and decay together, by allowing the top to go off-shell. Thus, in our computation we take into account the interference terms (also known as nonfactorizable corrections).

We shall perform this computation and present the results at the parton level only. Since the final state of the top quark pair production process is $bW^+\bar{b}W^-$ (at lowest order), the experimental signature is either 6 jets (if both W 's decay hadronically) or lepton(s) + jets + missing energy (if one or both W 's have semileptonic decays). We assume that the issues related to jet reconstruction and identification have been solved, and our final state contains two W bosons ², two

² At the Monte Carlo level, we actually allow the on-shell W 's to decay, either semileptonically

b quarks and possibly a gluon. Even at this level, the complete computation of all the diagrams contributing to this final state (Born and next to leading order) is a very difficult task. Therefore, we shall employ the double pole approximation (DPA) which means taking into account only the diagrams which contain a top - antitop pair.

It is worth mentioning a resemblance between the process of interest to us:

$$e^+e^- \rightarrow t \bar{t} (g) \rightarrow b W^+ \bar{b} W^- (g)$$

and the W pair production and decay process ($e^+e^- \rightarrow W^+ W^- \rightarrow 4f$) with QED corrections at LEP. The issues which arise in the two computations are similar, because in both cases we are dealing with the production and decay of heavy unstable particles. Our treatment is largely similar to the one used for the electroweak process [18], [19], [21]. But there are some differences, both in the implementation of the DPA approximation and in the number and type of terms which contribute to the final result (the latter being due to the fact that in our case the intermediate off-shell particles are fermions, and not bosons). These differences will be pointed out in the course of our discussion.

The outline of the thesis is as follows. In Chapter **2** we lay out the general framework in which we perform our computation. This includes a description of the double pole approximation (DPA) method for the top production and decay case, with an overview of the Feynman diagrams contributing to this process. We also discuss the computation of differential cross sections, with some details on the treatment of the infrared singularities, and we review some salient features of the treatment of the widths of unstable particles.

Chapter **3** is dedicated to an analysis of the top production and decay process or into a pair of massless quarks, but in the latter case we do not take into consideration QCD corrections to the W decay.

in conjunction with the radiation of a real (hard) gluon. We start with a description of the computation of the amplitudes contributing to this process. Since we perform a full off-shell computation, a prescription for separating the total amplitude into parts which can be associated with radiation in the production or decay stage is also given. Finally, we study the properties of gluon radiation, and the impact of the gluon on top mass reconstruction. Special attention is paid to the issue of interference between production- and decay-stage radiation, and the effect which it can have on differential distributions.

The computation of virtual corrections is the subject of Chapter 4. The evaluation of NLO amplitudes in the double pole approximation is presented and discussed in some detail. The results for the amplitudes corresponding to interference diagrams are similar to results previously obtained for the W pair production process, while for the vertex corrections and fermion self-energy diagrams there are differences between the two cases. In order to facilitate comparisons with the on-shell approach, we also formulate our results in terms of correction to the production and decay subprocesses and interference contributions. The gauge invariance of the total and partial amplitudes in DPA is manifest in this formulation. Results for this section include values for the total cross section and an analysis of the impact of interference effects on the invariant top mass distribution. Comparisons between our results and results obtained in an alternative approach (in which the real gluon interference terms are computed analytically) are also made.

We end in Chapter 5 with a summary and the conclusions. The Appendix contains some technical details related to our computation: we present a short description of the spinor techniques used to evaluate the amplitudes contributing to our process, expressions for these amplitudes, and details about the evaluation of virtual corrections with the help of Passarino-Veltman functions.

Chapter 2

Computational Approach

Our aim in this thesis is the evaluation of next-to-leading order amplitudes and differential cross sections for the top production and decay process at linear colliders. In this section, we start with a description of the general framework in which we perform our computation. The Feynman diagrams contributing to the process are introduced, and the double pole approximation is explained. Some general issues related to the evaluation of the cross section, the treatment of infrared singularities and the treatment of the top width are examined. Details about the evaluation of amplitudes and a comprehensive analysis of the specific issues arising in this computation can be found in later sections.

2.1 Amplitudes in DPA

In top pair production at linear colliders, what is actually observed experimentally is the process

$$e^+e^- \rightarrow b W^+ \bar{b} W^- \quad (2.1)$$

There are many diagrams contributing to this process. At tree level, they can be split into 3 classes: diagrams which contain a top-antitop pair (Fig. 2-1), diagrams which contain either one top quark or a top antiquark (Fig. 2-2 and charge conjugates), and diagrams which do not contain any top (there are about 50 such diagrams). Although not an easy task, it is possible to perform the evaluation of all these amplitudes (by using one of the automated tree level amplitude computation programs, like MADGRAPH [22]). The computation of QCD corrections to all tree level diagrams increases the degree of complexity by quite a lot, and is probably not feasible yet.

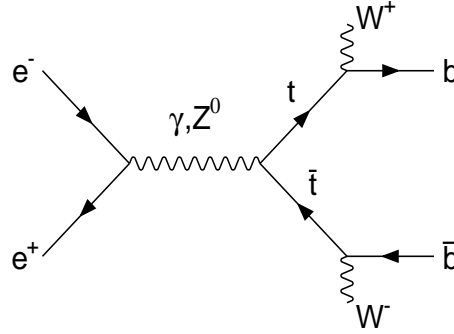


Figure 2-1: The top-antitop diagrams contributing to the process (2.1).

Fortunately, we can make use of the fact that, looking for top pair production, we are interested in a specific region of the final state phase space of (2.1). This region is defined by the requirement that the invariant mass of the $W b$ pair is close to the top mass: $p_t^2, p_{\bar{t}}^2 \approx m_t^2$, where $p_t = p_{W^+} + p_b$ and $p_{\bar{t}} = p_{W^-} + p_{\bar{b}}$ ¹. In this region, the amplitudes corresponding to the top-antitop diagrams are enhanced

¹ p_i are the four-momenta of the particles involved in the process; $p^\mu = (E; p_x, p_y, p_z)$ and $p^2 = p^\mu p_\mu = E^2 - p_x^2 - p_y^2 - p_z^2$ is a quantity invariant under Lorenz transformations. We also denote the antiquarks by a bar over the corresponding quark symbol.

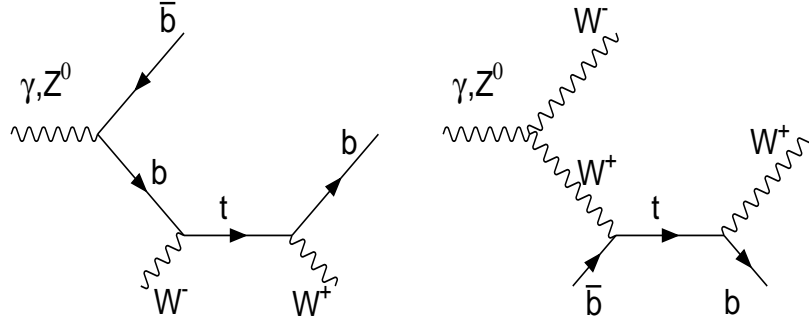


Figure 2-2: Single top diagrams contributing to the process (2.1).

by the two resonant propagators coming from the two intermediate top quarks:

$$\mathcal{M} \sim \frac{1}{p_t^2 - \bar{m}_t^2} \frac{1}{p_{\bar{t}}^2 - \bar{m}_t^2} \quad (2.2)$$

For this reason, the first class of diagrams (Fig. 2-1) are called doubly resonant diagrams. Correspondingly, the second class (Fig. 2-2) and the third class of diagrams, which contain only one top quark propagator or none, are called singly resonant and non-resonant diagrams respectively.

Note that the contributions coming from singly resonant diagrams (whose corresponding amplitudes contain a single resonant propagator) are *reduced* by a factor Γ_t/m_t with respect to the doubly resonant contributions. Therefore, in the first approximation we can neglect the singly-resonant and non-resonant diagrams; we shall use the *double pole approximation* (DPA) which means keeping only the amplitudes which have a doubly resonant behavior when the top and the antitop go on-shell.

At next to leading order, the diagrams contributing to the top production and decay process are presented in Figures 2-3 and 2-4. In Figure 2-3 we present the doubly-resonant diagrams contributing to the process with a real gluon in the final

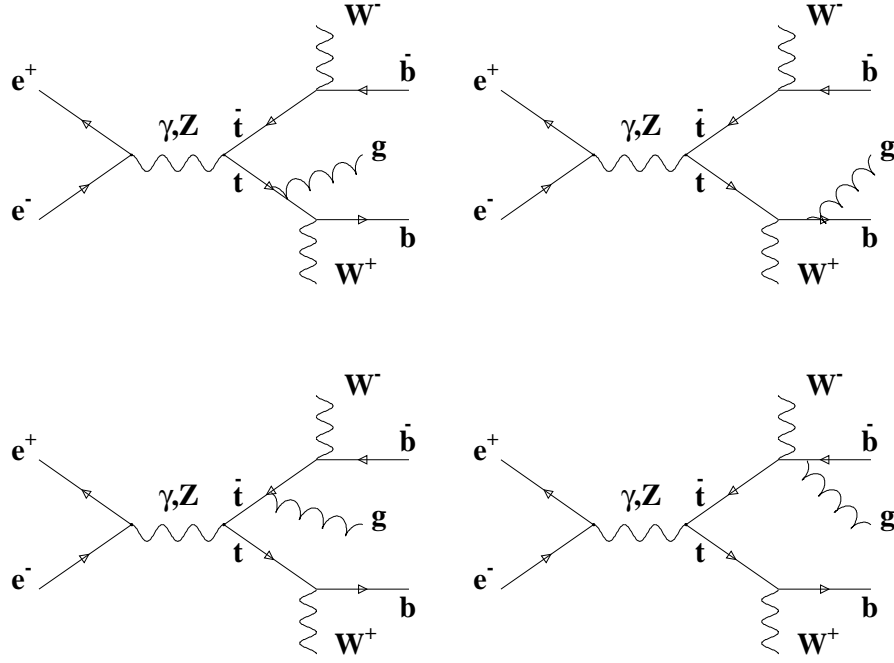


Figure 2-3: Feynman diagrams for gluon radiation in top production and decay.

state:

$$e^+e^- \rightarrow b W^+ \bar{b} W^- g \quad (2.3)$$

The DPA amplitude for this process can be written as a sum of four terms :

$$\mathcal{M}^{rg} = \mathcal{M}_t + \mathcal{M}_{\bar{t}} + \mathcal{M}_b + \mathcal{M}_{\bar{b}} \quad (2.4)$$

each term corresponding to one of the diagrams in Figure 2-3 (the subscript refers to the quark the gluon couples to).

Some of Feynman diagrams for virtual corrections to the tree level process are presented in Figure 2-4. These diagrams can be divided into two classes : correc-

tions to particular subprocesses – the vertex and fermion self-energy diagrams in Fig. 2-4 a) and b) respectively – and interference type corrections (Fig. 2-4 c) and d)). Strictly speaking, the vertex and self-energy diagrams also contribute to interference between subprocesses; but, for the sake of brevity, we shall refer to the diagram in Fig. 2-4 a) as the production vertex correction diagram, and so on. Also, in the following, we will denote the tree level amplitude (Fig. 2-1) by \mathcal{M}^0 , and the amplitude for the first order virtual corrections by \mathcal{M}^{vg} :

$$\mathcal{M}^{vg} = \mathcal{M}_{t\bar{t}} + \mathcal{M}_{tb} + \mathcal{M}_{t\bar{b}} + \mathcal{M}_{b\bar{t}} + \mathcal{M}_{t\bar{b}} + \mathcal{M}_{b\bar{b}} \quad (2.5)$$

Here, the first three terms correspond to the three off-shell vertex corrections (which include in a suitable way the fermion self-energies, as described in section 4.1.3), and the last three terms come from the interference diagrams.

2.2 Cross sections and infrared singularities

The partial amplitudes corresponding to the contributing Feynman diagrams are evaluated using spinor techniques (see Appendix A for details). The differential cross sections are obtained by taking the square of the total amplitude (sum of partial amplitudes) and summing over the polarizations (spins) of particles in the final state:

$$d\sigma^{0,vg,rg} \propto \sum_{polarizations} |\mathcal{M}^{0,vg,rg}|^2 \quad (2.6)$$

The proportionality constant contains phase space and kinematic factors and it is given in Appendix B. Our approach allows the computation of cross sections for particles of definite polarizations in the final state; but since these polarizations cannot be experimentally observed, all our results will be given with the spin sums in the final states performed.

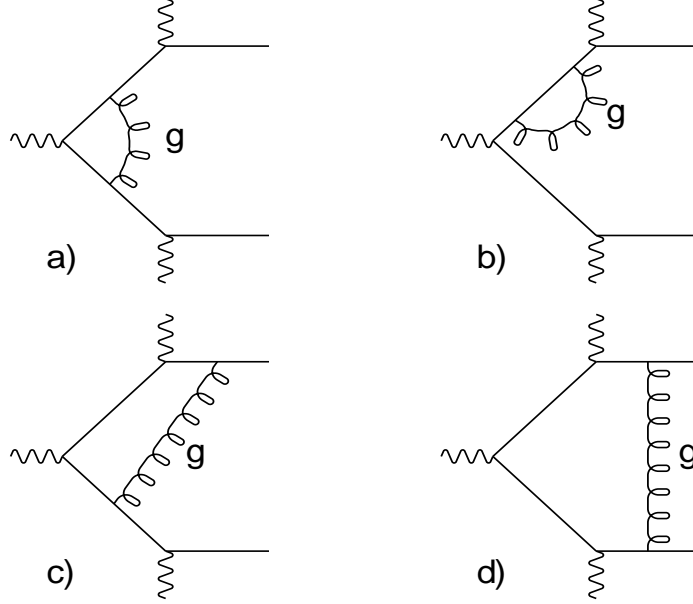


Figure 2-4: Feynman diagrams for virtual gluon corrections to top production and decay.

Our computations are relevant to two different experimental situations: the case when the final state contains only the b, \bar{b}, W^+ and W^- particles, and the case when besides these particles there is also a gluon. In the latter case, the only amplitudes which contribute are the amplitudes in Figure 2-3; the total cross section can be written as:

$$\sigma^{rg} \propto \int_{\epsilon_g > E_{cut}} |\mathcal{M}^{rg}|^2 d\Omega_{0+g} \quad (2.7)$$

(where Ω_0 is the phase space of the tree level process, and Ω_{0+g} is the phase space of the process with a real gluon radiated). Note that the integral is not performed over the entire phase space, but a lower limit E_{cut} on the gluon energy ϵ_g is imposed. The reasons for this cut are twofold: first, experimental: only gluons with energies greater than a certain threshold can be observed; second, theoretical:

when the gluon energy goes to zero, the amplitude \mathcal{M}^{rg} goes to infinity, and the cross section itself diverges. This is the well known issue of infrared singularities in the radiation of a massless boson. The way to deal with this divergent behavior is to note that it is not possible to observe gluons with arbitrarily low energy, no matter how good our detector performance. Therefore, the contribution to the cross section coming from infinitesimally small gluon energies should be added to the cross section for the process without a gluon in the final state ². Thus the infrared contributions coming from soft real gluon radiation cancel out the equal but opposite-sign infrared quantities which appear in the evaluation of the virtual corrections.

In consequence, the tree level diagrams (Fig. 2-1), the virtual corrections diagrams (Fig. 2-4) and the real gluon radiation diagrams (Fig. 2-3) all contribute to the NLO cross section for the process with the b, \bar{b}, W^+, W^- final state :

$$\sigma^1 \propto \int \left(|\mathcal{M}^0|^2 + 2\text{Re}[\mathcal{M}^0(\mathcal{M}^{vg})^*] \right) d\Omega_0 + \int_{\epsilon_g < E_{cut}} |\mathcal{M}^{rg}|^2 d\Omega_{0+g} \quad (2.8)$$

The cancellation of infrared divergences between the real gluon radiation and the virtual corrections part is performed by using the phase space slicing method. This method amounts to introducing a technical cut-off ϵ for the gluon energy; if the gluon energy is smaller than ϵ , the contribution \mathcal{M}^{rg} is evaluated in the soft gluon approximation. In this approximation the amplitude factorizes to the tree-level amplitude times an eikonal factor:

$$\mathcal{M}^{rg} = \mathcal{M}^0 \left(\frac{p_b^\mu}{kp_b} - \frac{p_{\bar{b}}^\mu}{kp_{\bar{b}}} \right) (-ig_s) \epsilon_{g\mu} = \mathcal{M}^0 B^\mu (-ig_s) \epsilon_{g\mu} \quad (2.9)$$

(only gluons radiated from the on-shell b quarks contribute to the infrared singularity, as opposed to the case of the on-shell approximation, when gluons radiated

²The solution to the problem of infrared divergences is due to Bloch and Nordsieck [24]; for a pedagogical introduction see [23]; a complete treatment including methods for evaluation the soft gluon integral in Eq. 2.10 can be found in [25].

from the top quarks also give rise to a singular behavior). The phase space also factorizes: $d\Omega_{0+g} = d\Omega_0 \times d\Omega_g$; therefore

$$\int_{\epsilon_g < \epsilon} |\mathcal{M}^{rg}|^2 d\Omega_{0+g} = \int |\mathcal{M}^0|^2 d\Omega_0 \times \left(\frac{\alpha_S}{\pi} \int_{\epsilon_g < \epsilon} \frac{d^3k}{4\pi\epsilon_g} (-1) B^\mu B_\mu \right) \quad (2.10)$$

The term in parentheses (let's call it $Y_{b\bar{b}}$), which describes the effects of soft gluon radiation, can then be computed independently of the tree level amplitude. Since it is infrared divergent, $Y_{b\bar{b}}$ is usually evaluated with the help of some regularization procedure (we use mass regularization, which means assuming that the gluon has an infinitesimally small mass μ). The same regularization procedure is used to compute the virtual corrections diagrams which are infrared divergent (in our case, the decay-decay interference diagram 2-4 d) and corrections to the self-energies of the b, \bar{b} quarks). The final result

$$\sigma^1 \propto \int \left(|\mathcal{M}^0|^2 (1 + Y_{b\bar{b}}) + 2\text{Re}[\mathcal{M}^0 (\mathcal{M}^{vg})^*] \right) d\Omega_0 + \int_{\epsilon < \epsilon_g < E_{cut}} |\mathcal{M}^{rg}|^2 d\Omega_{0+g} \quad (2.11)$$

is finite and independent of the value of the regularization parameter μ .

Finally, we shall make some comments on the choice of the ϵ and E_{cut} parameters. The E_{cut} is meant to separate between the experimentally observable gluons and those gluons soft enough to be undetectable in the experimental setup under use. For the detectors planned for an e^+e^- linear collider this would mean a value for E_{cut} of order 5 to 10 GeV.³ On the other hand, ϵ is an unphysical technical parameter needed to solve the infrared singularities problem. The only requirement on its value is that it is small enough so that the soft gluon approximation works. As we shall argue in section 4.4, this means that ϵ should be much smaller than the energy of the gluons which contribute to the interference (about 1.5 GeV). We therefore shall use for the technical cut ϵ values of order 0.1 GeV.

³More about our choice (as well as other cuts intended to select observable gluons) can be found in section 3.2

2.3 Top width and gauge invariance

The implementation of finite width for unstable particles is a delicate problem. If we use the zero order propagator for the top quark:

$$\mathcal{S}_0(p) = \frac{i}{\not{p} - m_0}$$

the amplitude for our process will have an unphysical non-integrable singularity in the region of the phase space where the top propagator becomes resonant. Hence the need to regularize this singularity by taking into account the unstable particle's width. However, the introduction of finite width tends to spoil gauge invariance. The reason for this is that our theory is gauge invariant *in fixed order in perturbation theory*. The introduction of the width, performed naturally through Dyson resummation ⁴:

$$\mathcal{S} = \mathcal{S}_0 + \mathcal{S}_0(-i\Sigma(\not{p}))\mathcal{S}_0 + \dots = \frac{i}{\not{p} - m_0 - \Sigma(\not{p})} \quad (2.12)$$

amounts to taking into account contributions coming from higher orders in perturbation theory. Therefore, gauge invariance problems might arise.

These issues have been first recognized and dealt with in processes where the role of unstable particles is played by gauge bosons. There are a variety of methods to restore gauge invariance in these cases; the fermion-loop scheme [26] is a favored one, although it is difficult to implement for complicated processes. For the W pair production process at LEP, a simpler prescription is available [18], [19], [21]. In the computation of the tree level DPA amplitude:

$$\mathcal{M}_{DPA} = \frac{\tilde{\mathcal{M}}(p_{W+}^2, p_{W-}^2)}{(p_{W+}^2 - M_W^2 + iM_W\Gamma_W)(p_{W-}^2 - M_W^2 + iM_W\Gamma_W)} \quad (2.13)$$

⁴ Here m_0 is the bare mass of the particle, while $\Sigma(\not{p})$ stands for the one-particle irreducible self-energy.

one evaluates the normalized amplitude $\tilde{\mathcal{M}}$ at the poles (that is, for on-shell W 's). The residue $\tilde{\mathcal{M}}(M_W^2, M_W^2)$ is gauge invariant, and the difference between this residue and the exact result is obviously non-doubly resonant, therefore it can be ignored within the DPA. Thus, in this approach the consequences of having off-shell particles are restricted to the denominators of the W gauge bosons propagators. Moreover, since the DPA radiative corrections to this process are proportional to the tree level amplitude, gauge invariance at NLO is insured also.

However, the issue of gauge invariance in the W pair production process appears even at tree level because of the fact that W is a *gauge boson*. In other words, the gauge invariance we are concerned with in Eq. 2.13 is invariance with respect to the W gauge. For the top production process, this issue does not arise; therefore we can compute the tree level amplitude \mathcal{M}_0 with off-shell momenta, and the result will be gauge independent because the top quark propagator does not depend on any gauge.

At next to leading order, though, the top quark can radiate a gluon (either real or virtual), and the problem of gauge invariance with respect to the gluon gauge arises. However, this is a quite different problem from the one discussed above; even in the W pair production case, at NLO gauge invariance with respect to the gauge of the radiated photon has to be treated separately. For QCD corrections to the top pair production case, we shall address this problem for both the case of real gluon radiation and virtual corrections in the appropriate chapters below.

There is one more issue related to the treatment of the unstable particle width. The width extracted from the imaginary part of the particle self-energy in Eq. 2.12 is a quantity dependent on the top energy – called the running width. In the W pair production process, it has been shown that the use of the running width generates problems at higher energies [18]. Another option is to use the fixed width obtained by evaluating the top decay width from the process $t \rightarrow bW(g)$,

and using this constant value in the top propagator. In the W case, it has been found preferable to use the *complex-mass scheme*, which replaces M_W^2 with the complex mass $\bar{M}^2 = M_W^2 - iM_W\Gamma_W$ not only in the denominator of the propagator, but also in the couplings of the particles to the gauge bosons (since these couplings can be treated as dependent on the M_W mass). In the top production case, the couplings do not depend on the top mass; so in our implementation, the top mass is replaced by the complex mass $\bar{m}_t^2 = m_t^2 - im_t\Gamma_t$ (here Γ_t is the constant next-to-leading order top width) in the top propagator denominators only.

Chapter 3

Real gluon radiation

Future high energy lepton colliders — e^+e^- and $\mu^+\mu^-$ — can provide relatively clean environments in which to study top quark physics. Although top production cross sections are likely to be lower at these machines than at hadron colliders, the color-singlet initial states give lepton machines some advantages. Furthermore, the fact that the laboratory and hard process center-of-mass frames coincide greatly simplifies the reconstruction of final states. In addition, many of the top quark's couplings, especially those to the photon and Z^0 boson, can be easily studied there.

The potential for precision studies of top physics at such colliders requires precision predictions from the theory, beyond leading order in perturbation theory. In particular, QCD corrections must be taken into account. One effect of the QCD interaction is the radiation of a real gluon. This process can have a sizable impact on the analysis of the top production and decay final state variables. Jets from radiated gluons can be indistinguishable from quark jets, complicating identification of top quark events from reconstruction of top's decay products. To make matters worse, emission may occur in either the top production or decay

processes, so that radiated gluons may or may not themselves be products of the decay. Subsequent mass measurements can be degraded, not only from misidentification of jets but also from subtle effects such as jet broadening when gluons are emitted near other partons.

In this section we study the effects of real gluons radiated in top quark production and decay at e^+e^- colliders [29]. We consider collision energies well above the top pair production threshold, so although for definiteness we will refer to electrons in the initial state, our parton-level results apply equally well to $\mu^+\mu^-$ collisions at the same energy. We allow for the top quarks to be off-shell, keeping the full width-dependent top propagator and retaining all spin correlations. Gluon radiation for off-shell top has been treated previously in the soft gluon approximation [27, 28]. Here we give an exact treatment for arbitrary gluon energies. We study properties of the radiated gluons, top mass reconstruction, and effects of interference between production- and decay-stage gluons that can be sensitive to the top quark width.

3.1 Amplitude evaluation

Our aim is to evaluate the differential cross section for real gluon emission in top quark production and decay:

$$e^+e^- \rightarrow \gamma^*, Z^* \rightarrow t\bar{t}(g) \rightarrow bW^+\bar{b}W^-g. \quad (3.1)$$

In top events at e^+e^- colliders, there are no gluons radiated from the color-singlet initial state. Final-state gluon emission can occur in both the production and decay processes, with gluons radiated from the top or bottom quarks (or antiquarks), as shown in Figure 2-3.

For purposes related to top mass reconstruction, it is desirable to be able to

associate the radiated gluon with either the top production process or the decay process. While trivial in the on-shell approach, it is not possible to make this differentiation with 100% certainty if the top is allowed to be off-shell. However, we can use a sensible, *ad hoc*, definition: if the top is closer to its on-shell mass after the gluon has been emitted, call that production stage radiation; otherwise, call it decay stage radiation. Thus, emission from the top quark contributes to both production- and decay-stage radiation, depending on when the top quark goes on-shell. Emission from the b quarks contributes to decay-stage radiation only. The separation of these contributions at the amplitude level will be discussed below.

We compute the exact quantum mechanical amplitudes (also called matrix elements) for the diagrams shown in Figure 2-3 with all spin correlations and the bottom mass included, using the helicity methods of Kleiss and Stirling [30]. Working at the matrix element, rather than the matrix element squared, level has the usual advantages of numerical efficiency, and in our case has the additional advantage that we can identify individual contributions as well as interference between them. The explicit expressions for the matrix elements are complicated and not particularly illuminating, so we do not reproduce them here¹. A general overview including some specific details concerning this computation can be found in the appendix.

We do not assume the top quark to be on-shell; therefore we keep the finite top width Γ_t in the top quark propagator and include all interferences between diagrams. We use exact kinematics in all parts of the calculation. We do not include radiation from hadronic W decays; the W bosons are assumed to decay leptonically and we integrate over the decay products in the results presented here. In practice, radiative hadronic W decays should probably be taken care of

¹A FORTRAN program containing the matrix elements can be obtained from the author.

at the level of jet fragmentation simulations; but this requires a separate study.

3.1.1 Production–decay decomposition

As mentioned above, calculating at the amplitude level allows us to identify contributions from individual processes and their interferences. We are particularly interested in distinguishing between contributions from gluons radiated in the top quark production and decay stages. This is directly related to reconstruction of the top quark momentum from its decay products, which in an experiment allows us both to identify top events and to measure m_t . The presence of gluon radiation complicates the reconstruction because the emitted gluon may or may not be part of the top decay. If the gluon is not part of the decay, then it represents a correction to top production and should not be included in the top momentum reconstruction:

$$m_t^2 \approx p_t^2 = (p_b + p_W)^2 \equiv p_{bW}^2 . \quad (3.2)$$

(The use of the \approx sign in the above equation signifies that the sum squared of the 4-momenta of the top decay products – for which we will use the shorthand p_{Wb} – is close to the top mass squared.) If on the other hand the gluon is part of the decay, then it *should* be included in top reconstruction:

$$m_t^2 \approx p_{tg}^2 = (p_b + p_W + p_g)^2 \equiv p_{bWg}^2 . \quad (3.3)$$

Being able to make this distinction turns out to be useful for purposes of efficient phase-space integration as well.

Although this production–decay distinction cannot be made absolutely in an experiment², the various contributions can be separated in the calculation. For radiation from the b and \bar{b} quarks, the assignment is easy: these contributions,

²If the interference between processes is large this distinction is not even meaningful.

corresponding to the two right-hand diagrams in Fig. 2-3, are clearly part of the top quark decay. However, as noted above, gluon emission from the top quark (or antiquark) contributes to both the production and decay stages; which is which depends on whether the top was closer to its mass shell before or after emitting the gluon. This condition corresponds to which of the two propagators from the top that emitted the gluon is numerically larger.

We can make the separation in our calculation as follows [28]. For definiteness, we consider gluon emission from the top quark, shown in the upper left diagram in Fig. 2-3. The matrix element for this diagram contains propagators for the top quark both before and after it radiates the gluon. The matrix element therefore contains the factors

$$\mathcal{M}_t \propto \left(\frac{1}{p_{Wb}^2 - m_t^2 + im_t\Gamma_t} \right) \left(\frac{1}{p_{Wb}^2 - m_t^2 + im_t\Gamma_t} \right). \quad (3.4)$$

The right-hand side can be rearranged to give

$$\mathcal{M}_t \propto \frac{1}{2p_{Wb} * p_g} \left(\frac{1}{p_{Wb}^2 - m_t^2 + im_t\Gamma_t} - \frac{1}{p_{Wbg}^2 - m_t^2 + im_t\Gamma_t} \right). \quad (3.5)$$

This separates the production and decay contributions to the matrix element. The first term in parentheses contains a propagator that peaks when $p_{Wb}^2 = m_t^2$, which corresponds to the condition for production stage, as in Eq. 3.2. Similarly, the second term peaks for $p_{Wbg}^2 = m_t^2$, which corresponds to decay emission as in Eq. 3.3.

The complete amplitude in Eq. 2.4 can now be rewritten schematically as ³

$$\mathcal{M}^{rg} = \mathcal{M}_{prod} + \mathcal{M}_{tdecay} + \mathcal{M}_{idecay}. \quad (3.6)$$

The cross section, obtained from taking the absolute square of \mathcal{M}^{rg} , then contains separate production and decay contributions, from $|\mathcal{M}_{prod}|^2$ and $|\mathcal{M}_{tdecay}|^2$,

³Expressions for the partial amplitudes can be found in Appendix B.

$|\mathcal{M}_{\bar{t}decay}|^2$, respectively. It also contains cross terms representing the interferences, which in principle confound the separation but in practice are quite small.

The interference terms *are* interesting in their own right, although not for top reconstruction. In particular, the interference between production- and decay-stage radiation can be sensitive to the top quark width Γ_t [27, 28], which is 1.42 GeV in the Standard Model at $\mathcal{O}(\alpha_s)$ [6]. The interference between for example the two propagators shown in Eq. 3.5 can be thought of as giving rise to two overlapping Breit-Wigner resonances. The peaks are separated roughly by the gluon energy, and each curve has width Γ_t . Therefore when the gluon energy becomes comparable to the top width, the two Breit-Wigners overlap and there can be substantial interference. In contrast, if the gluon energy is much larger than Γ_t , the overlap — and hence the interference — is negligible. Therefore the amount of interference serves as a measure of the top width. We will explore this more below.

3.1.2 Gauge invariance

Since gauge bosons contribute to the processes analyzed in this thesis, it is natural to consider the issue of gauge invariance. In order to perform our computations, it is necessary to choose some gauge for the bosons involved (for example, the propagators for the γ, Z_0 bosons are computed the Feynman gauge, while the definition of the gluon polarization vector depends on a gauge parameter as described in the appendix). While our choice of gauge may vary, the final results should be independent of this choice.

Due to the fact that the electrons in the initial state are considered massless, there is no amplitude dependence on the gauge in which we evaluate the γ, Z_0 propagators. However, this is not true anymore for the case of the gluon gauge.

This has to do with the fact that the top quarks can be off-shell; it is an easy exercise showing that amplitudes in the on-shell approximation are independent of the gluon gauge. More precisely, the reason that gauge invariance is lost is that the physical process we actually compute is:

$$e^+e^- \rightarrow b W^+ \bar{b} W^- g \quad (3.7)$$

and to obtain a gauge invariant result we should take into account all the Feynman diagrams contributing to this final state. Since our computation includes only diagrams with two intermediate top quarks, the final result is not strictly gauge invariant.

However, the diagrams we take into consideration are the only ones from the set contributing to (3.7) which have a doubly resonant structure. So, if one considers the gauge invariant result as being a sum of doubly-resonant, singly resonant and nonresonant terms, the only diagrams which can contribute doubly resonant terms are the diagrams containing two top quarks in Figure 2-3. Therefore, the amplitude in (3.6) differs from the gauge invariant result by singly or non-resonant terms only. This means that by subtracting non-doubly resonant terms from \mathcal{M}_{tot} (which is allowed in DPA) we can obtain a gauge invariant answer.

One way to perform these subtractions is as follows. Consider the diagram where the gluon is radiated by the top quark (the first diagram in Fig. 2-3). The contribution of this diagram to the production amplitude is:

$$\mathcal{M}_{prod}^{(t)} \sim \frac{1}{2kp_t} \bar{u}(b) \not{\epsilon}_W \frac{\not{p}_{Wb} + m_t}{p_{Wb}^2 - \bar{m}_t^2} \not{\epsilon}_g (\not{p}_{Wb} + \not{k} + m_t) \dots v(\bar{b}) . \quad (3.8)$$

By commuting $\not{\epsilon}_g$ to the right, this can be written

$$\mathcal{M}_{prod}^{(t)} \sim \frac{1}{2kp_t} \bar{u}(b) \not{\epsilon}_W \frac{(\not{p}_{Wb} + m_t)(2\epsilon_g \cdot p_{Wb} + \not{\epsilon}_g \not{k}) - (p_{Wb}^2 - m_t^2) \not{\epsilon}_g}{p_{Wb}^2 - \bar{m}_t^2} \dots v(\bar{b}) . \quad (3.9)$$

The term which breaks gauge invariance here is the one proportional to $(p_{Wb}^2 - m_t^2)$. This is a non-resonant term, regardless of the gluon being radiated in the production or decay stage (in other words, regardless of $p_{Wb}^2 \approx m_t^2$ or $p_{Wbg}^2 \approx m_t^2$); therefore, in keeping with the approximation used, we can neglect it.

A similar analysis works for the contribution of this diagram to the top decay amplitude. Starting with the expression:

$$\mathcal{M}_{tdecay}^{(t)} \sim \frac{-1}{2kp_t} \bar{u}(b) \not{\epsilon}_W \frac{\not{p}_{Wbg} - \not{k} + m_t}{p_{Wbg}^2 - \bar{m}_t^2} \not{\epsilon}_g (\not{p}_{Wbg} + m_t) \dots v(\bar{b}) \quad (3.10)$$

by commuting $\not{\epsilon}_g$ to the left, we obtain:

$$\mathcal{M}_{tdecay}^{(t)} \sim \frac{1}{2kp_t} \bar{u}(b) \not{\epsilon}_W \frac{\not{\epsilon}_g(p_{Wbg}^2 - m_t^2) - (2\epsilon_g \cdot p_{Wbg} - \not{k} \not{\epsilon}_g)(\not{p}_{Wbg} + m_t)}{p_{Wbg}^2 - \bar{m}_t^2} \dots v(\bar{b}) \quad (3.11)$$

and in this case we drop the term proportional to $(p_{Wbg}^2 - m_t^2)$. Finally, the amplitudes corresponding to the diagram in which the gluon originates from the \bar{t} can be computed in the same manner. The final result is gauge invariant, and differs from the exact result by non-doubly-resonant terms, as we have shown.

We have implemented the above computation in the Monte Carlo program, and have checked numerically that the difference between the gauge invariant result and the exact result is very small (of order 0.01% of the total cross section, and order 1% with respect to the interference terms). This indicates that the other non-doubly resonant contributions (coming from diagrams with a single top or none) are also small; a more detailed study is in progress.

Finally, we note that this method for restoring gauge invariance is not unique. We could, for example, have instead replaced the top mass in the top propagator numerator with the invariant masses: $\sqrt{p_{Wb}^2}$ in the production amplitude, and $\sqrt{p_{Wbg}^2}$ in the decay amplitudes. The result obtained with this method is also gauge invariant, and also differs from the exact result by non-resonant terms.

3.1.3 Monte Carlo and phase space integration

The integration over the final state phase space to obtain the cross section involves an integrand that contains multiple Breit-Wigner peaks from the top quark propagators as well as infrared singularities when the gluon energy becomes small. Even with cuts on E_g , the rapid variation of the integrand can spoil the integration procedure. To eliminate this problem, we tailor the momentum generator to the production of a gluon in association with two massive particles ($\gamma^*, Z^* \rightarrow t\bar{t}g$ or $t \rightarrow bWg$). The multiple Breit-Wigner peaks are taken into account by using a multi-channel approach that integrates separately over the individual production and decay contributions; the Breit-Wigner behavior is smoothed out in the phase space generation. The interference terms, which have products of Breit-Wigners that peak in different places, much like in Eq. 3.4, are integrated using a combination of the three main channels.

3.2 Numerical Results

In this section we show results of the numerical calculation described above. We present the cross section for $b\bar{b}W^+W^-g$ production in e^+e^- collisions at a 500 GeV center-of-mass energy, with a few exceptions which are clearly identified. The calculation is entirely at the parton level, and we do not include initial state radiation, beam energy spread, or beamstrahlung. We use the following numerical values of parameters: $m_t = 175$ GeV, $m_b = 5$ GeV, $M_W = 80$ GeV, $\Gamma_t = 1.42$ GeV, and $\alpha_s = 0.1$. Note that for the results presented in this section α_s appears simply as an overall factor, because all of our events contain a gluon.

Unless otherwise indicated, we use the following cuts. We require $E_g > 5$ GeV to eliminate the infrared singularity and because we intend for the gluon to be

detectable. In addition we wish the gluon to be separable from the b and \bar{b} quarks; this is implemented via the requirement $m_{bg}, m_{\bar{b}g} > 10 \text{ GeV}$, which we shall identify below as “ m_{bg} cuts.” (Separation could also be achieved with a cut on the gluon’s transverse energy E_T with respect to the b or \bar{b} ; the choice makes little difference in the resulting distributions.) In order to make sure that we do not get contributions to our results from regions of the phase space where non-doubly-resonant diagrams might be important, we require

$$160 \text{ GeV} \leq m_{bW} \leq 190 \text{ GeV} \quad \text{or} \quad 160 \text{ GeV} \leq m_{bWg} \leq 190 \text{ GeV} \quad (3.12)$$

and the same thing for the \bar{b} . These conditions will be identified as “ m_t cuts” below.

3.2.1 Characteristics of the gluon radiation

We begin with the relative contributions of production- and decay-stage radiation to the total cross section. Figure 3-1 shows the fraction of the total cross section due to production stage emission in events with an extra gluon, as a function of the minimum energy of the gluon. This figure contains no cuts besides that for gluon energy and is simply meant to illustrate how radiation is apportioned in top production and decay for different center-of-mass energies; the solid line corresponds to c.m. energy 1 TeV, and the dashed line is for 500 GeV. Both curves fall off as the minimum gluon energy increases; this reflects the decrease in phase space for gluons radiated in the production stage. We see that the production fraction is always higher at 1 TeV collision energy than at 500 GeV. This too reflects phase space — for a given gluon energy there is more phase space available to produce gluons in association with top pairs at the higher c.m. energy. However both fractions remain below 0.5; decay-stage radiation always dominates at these energies.

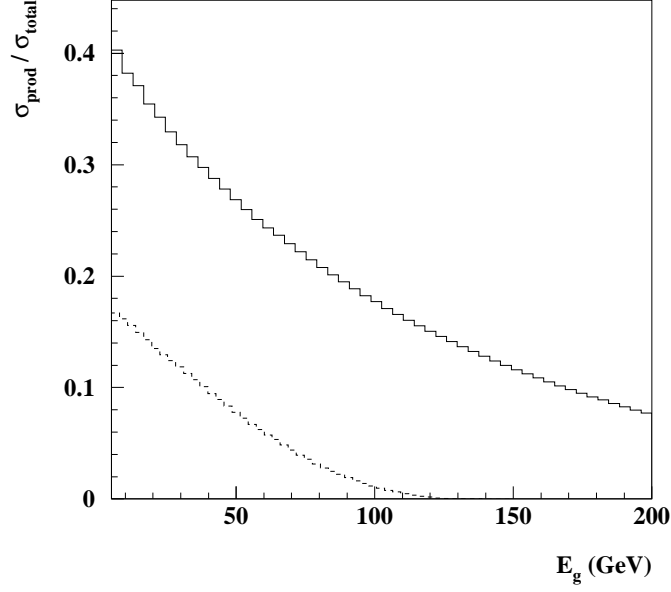


Figure 3-1: The fraction of gluon emissions radiated in the production stage, as a function of minimum gluon energy, for center-of-mass energy 1 TeV (solid line) and 500 GeV (dashed line), with no cuts.

Figure 3-2 shows for a 500 GeV center-of-mass energy the effect on the production fraction of separation cuts between the gluon and b quarks. The dashed line shows the fraction with no cuts. The dotted line corresponds to requiring that the transverse energy of the gluon with respect to the b and \bar{b} — which we denote $E_T(g, b)$ — be greater than 3 GeV. The solid line corresponds to the cut $m_{bg} > 10$ GeV where the b can either be a quark or antiquark. The effect of both of these cuts is to eliminate gluons that are soft and/or close to one of the bottom quarks; since these contributions tend to come from decay-stage radiation, their

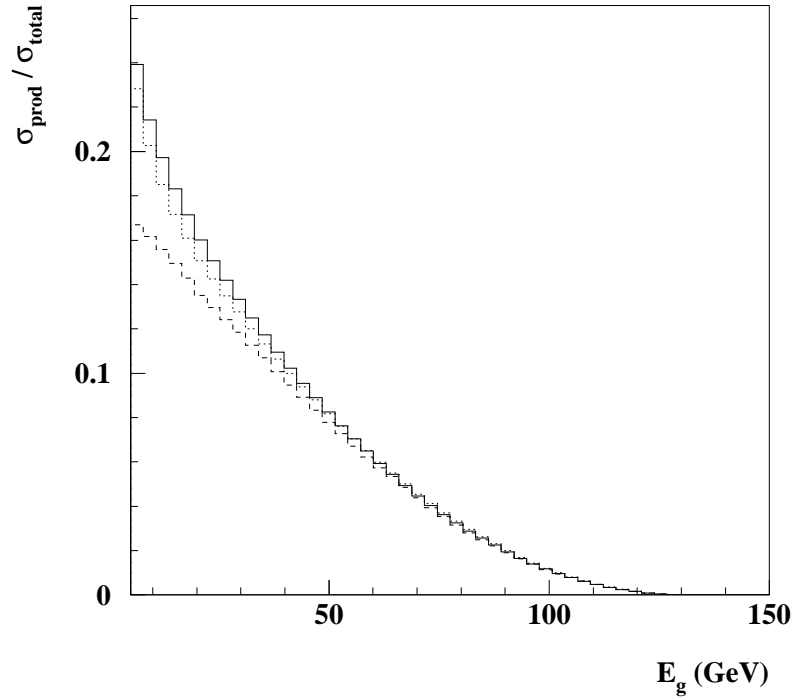


Figure 3-2: The fraction of gluon emissions radiated in the production stage, as a function of minimum gluon energy, for center-of-mass energy 500 GeV, with no cuts (dashed line), $E_T(g, b) > 3$ GeV (dotted line), and $m_{bg} > 10$ GeV (solid line).

effect is to increase the fraction of production-stage radiation. If the b were massless there would be a collinear singularity in the decay contribution; this does not happen in our case but the decay distribution still peaks when the b -quark–gluon angle is small. The effects of both cuts become smaller with increasing gluon energy.

Figure 3-3 shows the total gluon energy spectrum for a collision energy of

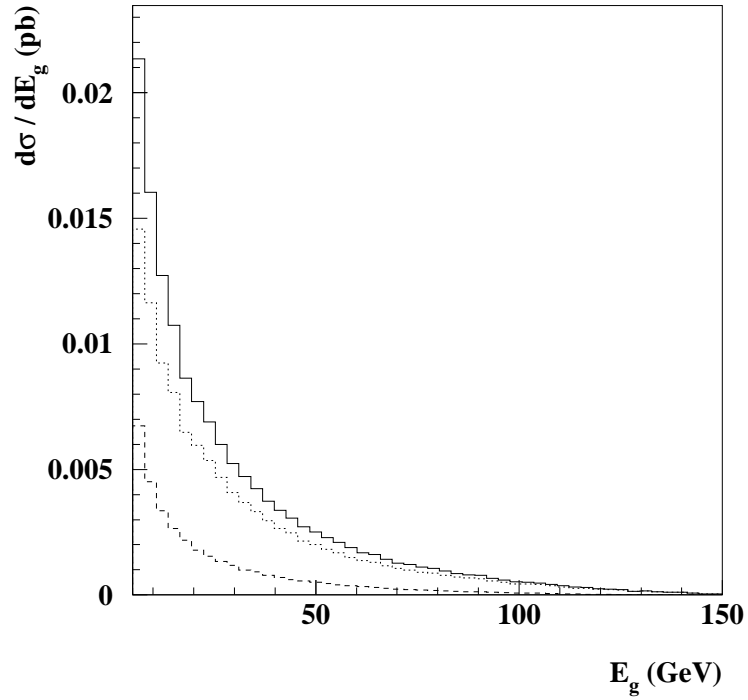


Figure 3-3: The spectrum of radiated gluons as a function of gluon energy in GeV for center-of-mass energy 500 GeV, with m_{bg} and m_t cuts (see text). Dashed histogram: production-stage radiation. Dotted histogram: decay-stage radiation. Solid histogram: total.

500 GeV along with its decomposition into production (dashed histogram) and decay (dotted histogram) contributions. The interferences between the two are negligible and are not shown; this will be true for all subsequent figures until we consider the interference explicitly. Included in this figure are the m_t and m_{bg} cuts discussed above. As indicated in the previous figures, radiation from the top

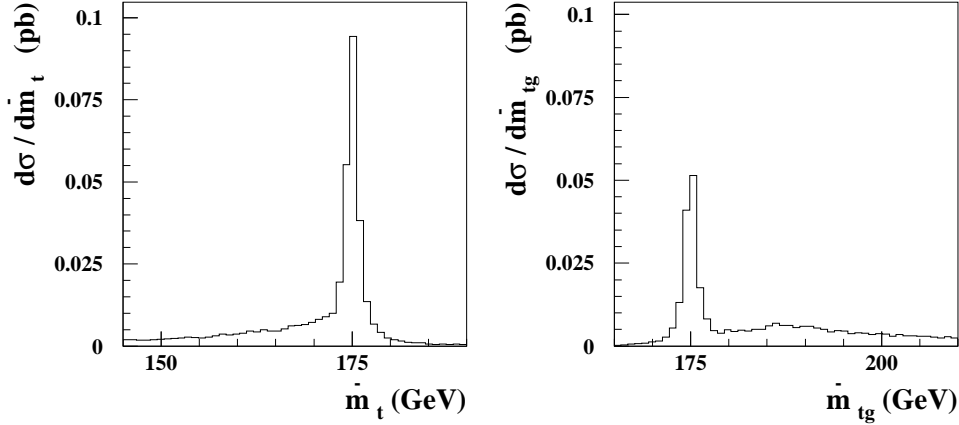


Figure 3-4: The top invariant mass spectrum without (left) and with (right) the gluon momentum included, for center-of-mass energy 500 GeV, with m_{bg} cuts and $E_g > 5$ GeV.

decays dominates. Otherwise the spectra are not vastly different; both exhibit the rise at low energies due to the infrared singularity characteristic of gluon emission, and both fall off at high energies as phase space runs out.

3.2.2 Mass Reconstruction

We now turn to the question of top mass reconstruction in the case when there is a gluon in the final state (more about measuring the top mass can be found in the next chapter). Figure 3-4 shows top invariant mass distributions with and without the extra gluon included; the first plot shows the distribution in m_{bW} and the second shows m_{bWg} . We have imposed m_{bg} cuts and required $E_g > 5$ GeV. In both cases there is a clear peak at the correct value of m_t . Note that the peak in the first plot contains the production contribution as expected, but the radiative decay part contributes as well. This is because even for decay-stage radiation, only one of the produced t quarks decays radiatively; the other still has $p_t^2 = p_{bW}^2$ and

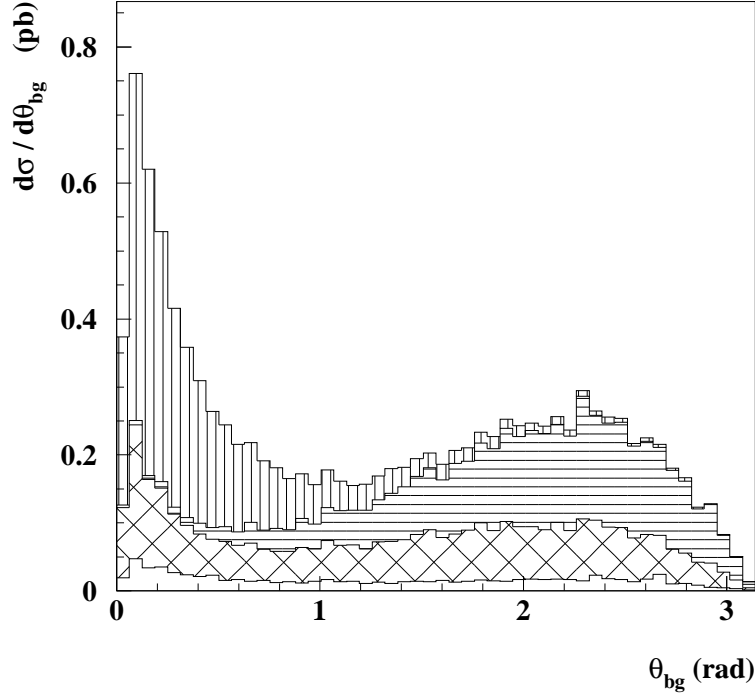


Figure 3-5: The distribution in the angle between the gluon and the b quark for center-of-mass energy 500 GeV, with $E_g > 5$ GeV. The various contributions are as described in the text.

therefore contributes to the m_{bW} peak. The long tails in the two distributions are from misassignments of the gluons. In the left-hand plot, where the gluon is not included in the reconstruction, we see a low-side tail due to events where the gluon was radiated in the decay but was not included in the reconstruction. Similarly, in the right-hand plot we see a high-side tail due to events where the gluon was radiated in association with production, and was included when it should not have been.

We wish to define a single distribution for the top mass that combines both types of events yet omits wrong combinations as much as possible. One possibility is to cut on the angle between the gluon and the b quark, whose distribution we show in Figure 3-5. This is motivated by the fact that gluons radiated from the b quarks are always part of the decay, and such gluons tend to be emitted close to the b quark direction. As we have mentioned, the mass of the b quark prevents a collinear singularity, but the gluon distribution still peaks close to the b , as can be seen in the figure. Because we wish to define cuts that give a narrow top invariant mass distribution, the distribution in θ_{bg} is decomposed into various invariant mass regions. (Here we refer to the b quark only, and not the \bar{b} .) Using the variables $\tilde{m}_t = m_{bW^+}$, $\tilde{m}_{tg} = m_{bW^+g}$, $\tilde{m}_{\bar{t}} = m_{\bar{b}W^-}$ and $\tilde{m}_{\bar{t}g} = m_{\bar{b}W^-g}$ we define four types of events:

- type 1 : $172 \text{ GeV} < \tilde{m}_{tg}, \tilde{m}_{\bar{t}} < 178 \text{ GeV}$ (vertical hatching)
- type 2 : $172 \text{ GeV} < \tilde{m}_t, \tilde{m}_{\bar{t}g} < 178 \text{ GeV}$ (horizontal hatching)
- type 3 : $172 \text{ GeV} < \tilde{m}_t, \tilde{m}_{\bar{t}} < 178 \text{ GeV}$ (cross hatching)
- type 4 : any other event (no hatching)

Type 1 events are dominated by contributions from radiative t decays, and we can see that they do tend towards the b quark direction. Type 2 events (horizontal hatching) are in turn dominated by radiative \bar{t} decays; gluons in this case tend to cluster near the \bar{b} direction, and since the b and \bar{b} tend to appear in opposite hemispheres, type 2 gluons are mostly found at large angles to the b . Events of type 3 (cross hatching) are mostly production-stage contributions; their distribution is more or less uniform, independent of the b quark direction. Finally, events of type 4 (no hatching) get contributions from both production and decay, with no compelling evidence for one over the other.

Using this figure we can make the following conventions:

- if $\theta_{bg} < 0.7 \text{ rad}$, assign gluon to t decay

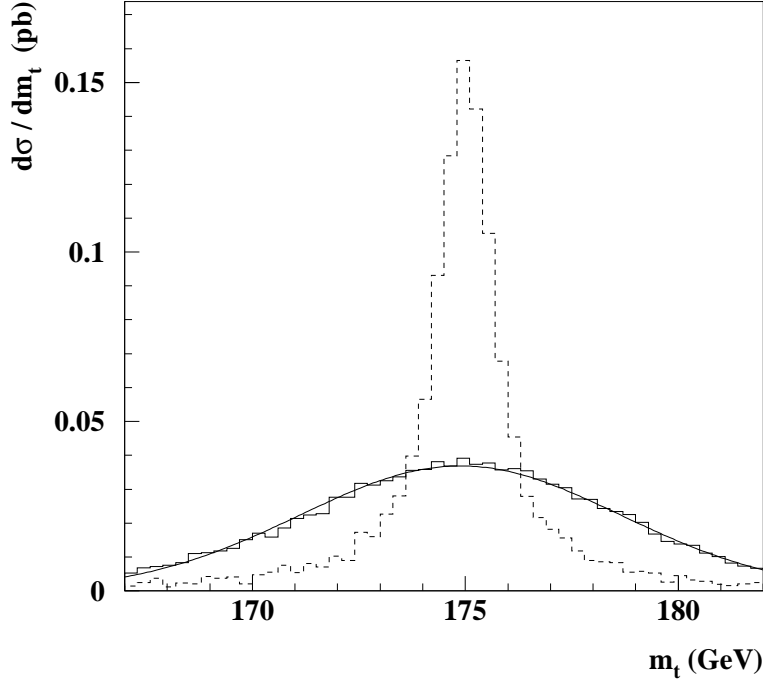


Figure 3-6: The top invariant mass spectrum with b -gluon angle selection criteria (dotted histogram), for center-of-mass energy 500 GeV, minimum gluon energy 5 GeV, and m_{bg} cuts. The solid curve and histogram show the effects of energy smearing.

if $\theta_{\bar{t}g} < 0.7$ rad, assign gluon to \bar{t} decay

if $\theta_{bg}, \theta_{\bar{b}g} > 1$ rad, assign gluon to $t\bar{t}$ production.

With these cuts on the proximity of the gluon to the b quark, we construct the top mass distribution presented in the dotted histogram in Figure 3-6.

Of course an important reason the cuts are so effective is that we work at the parton level. The experimentalists do not have that luxury, and, as one would expect, hadronization and detector effects are likely to cloud the picture. The solid

histogram in Fig. 3-6 shows the mass distribution after including energy smearing; the solid curve is a Breit-Wigner fit. The spread in the measured momenta of the final state particles is parametrized by Gaussians with widths $\sigma = 0.4\sqrt{E}$ for quarks and gluon, and $\sigma = 0.15\sqrt{E}$ for the W 's. We see that the central value does not shift, but the distribution becomes significantly wider.

These results are meant to give an indication of the effects of hard gluon radiation on mass reconstruction and how they might be dealt with. Other variables to consider in choosing the cuts are m_{bg} , the transverse energy of the gluon with respect to the b or \bar{b} , or some combination of energies and angles as defined in the various algorithms used in jet definitions for e^+e^- colliders. At tree level and with partons only, the exact choice is not very important. We will revisit the question in more detail when we include virtual corrections in a full NLO calculation.

3.2.3 Interference and Sensitivity to Γ_t

Finally, we return to the subject of interference. As mentioned above, the interference between the production- and decay-stage radiation can be substantial for gluon energies close to the total width of the top quark Γ_t ; the interference is therefore sensitive to the value of Γ_t . However, because this interference is in general small, we need to find regions of phase space where it is enhanced. This question was considered in [28] in the soft gluon approximation⁴, where it was found that the interference was enhanced when there was a large angular separation between the t quarks and their daughter b 's.

Here we examine whether the result of [28], which considered a fixed final-state configuration, survives the exact calculation and phase space integration. Figure 3-7 shows that it does. There we plot the distribution in the angle between the

⁴See also [27, 31]

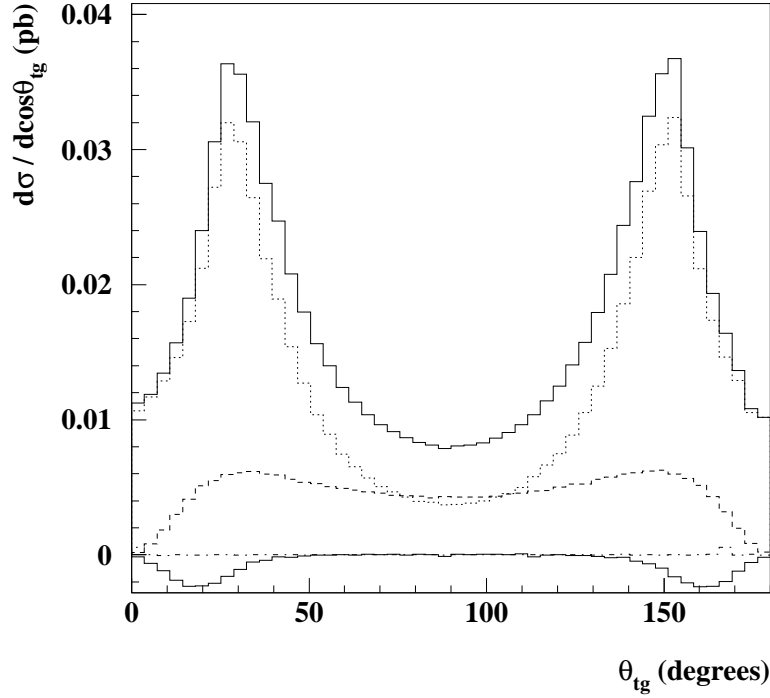


Figure 3-7: The distribution in angle between the top quark and the gluon for gluon energies from 5 to 10 GeV, $\cos \theta_{tb}, \cos \theta_{t\bar{b}} < 0.9$, m_t cuts, and 750 GeV collision energy. The upper solid histogram is the total and the other histograms represent the individual contributions: dotted: decay; dashed: production; dot-dashed: decay-decay interference; solid: production-decay interference.

emitted gluon and the top quark for gluon energies between 5 and 10 GeV and with $\cos \theta_{tb} < 0.9$ and m_t cuts. The center-of-mass energy is 750 GeV. This c.m. energy is chosen because for there to be significant interference between production and decay-stage radiation, both contributions must be sizable. At 500 GeV, we see from Figs. 3-1 and 3-2 that the production contribution is suppressed compared to

that from decay; as a result, the interference is very small. Increasing the energy increases the production-stage contribution. We note that the distributions at 750 GeV and 1 TeV do not differ substantially.

The histograms in Fig. 3-7 show the decomposition into the various contributions. The production-stage radiation is shown as a dashed histogram; we see that it reaches its largest values at relatively small and large angles. Small angles correspond to the t direction, and large angles more or less to the \bar{t} direction, since for the small gluon energies of interest here, the t and \bar{t} are nearly back-to-back. The dotted histogram represents the decay-stage contribution; it dominates the cross section and peaks in the same region as the production contribution. This leads to substantial production-decay interference, shown as the negative solid histogram. This interference is destructive, so that it serves to *suppress* the total cross section, shown as the positive solid histogram. This effect would be enhanced if we lowered the gluon energies to values closer to Γ_t , but jets from very low energy gluons are not likely to be observable, so we cut off the gluon energy at 5 GeV. Finally, interference between the emissions in the t and \bar{t} decays are shown as a dot-dashed histogram, but as there is very little overlap between the two phase space regions even with these cuts, this contribution is negligible.

The cuts we have used are fairly generic; we can further enhance the interference terms with a judicious choice of additional cuts. If we examine their behavior in more detail in various regions of phase space, we find that the sign of the interference terms depends on the value of the invariant mass of the top quark. Since we integrate over this mass, we get cancellations (a similar effect ensures cancellations of non-factorizable corrections in inclusive quantities).

Consider the interference between radiation in the production stage and the top decay stage. The product of the two Breit-Wigner peaks is proportional to

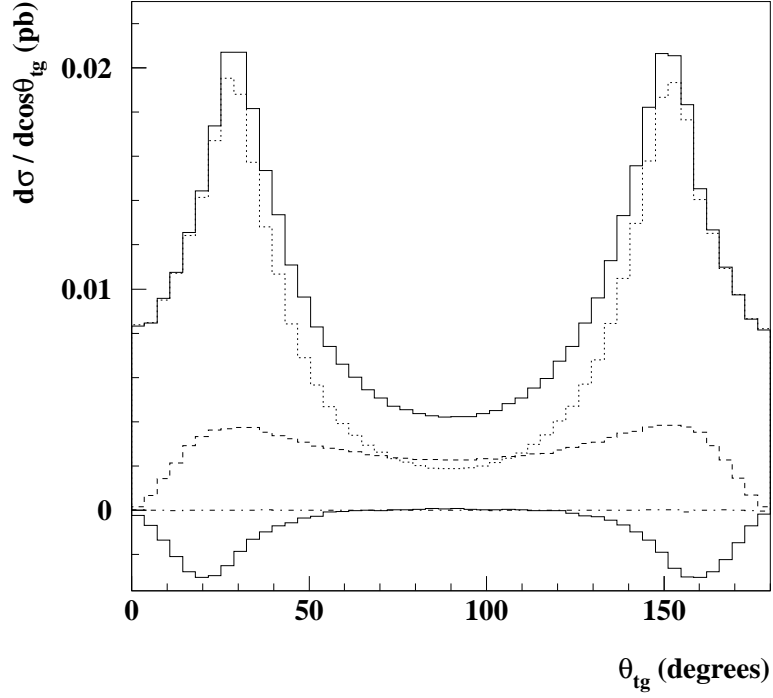


Figure 3-8: As in Fig. 3-7, with the addition of the cuts given in Eqs. 3.14,3.15.

the factor

$$f_t = (p_{Wb}^2 - m_t^2) * (p_{Wbg}^2 - m_t^2) + m_t^2 \Gamma_t^2 \quad (3.13)$$

This factor will multiply a quantity which, upon integration over angles, is negative. Therefore, for invariant mass values such that f_t is positive, the interference terms are negative, while for negative f_t , the interference terms are positive. We can impose cuts that take advantage of this: if we require the invariant masses to satisfy

$$f_t > 0, \text{ if } \theta_{bg} < \theta_{bg}; \quad (3.14)$$

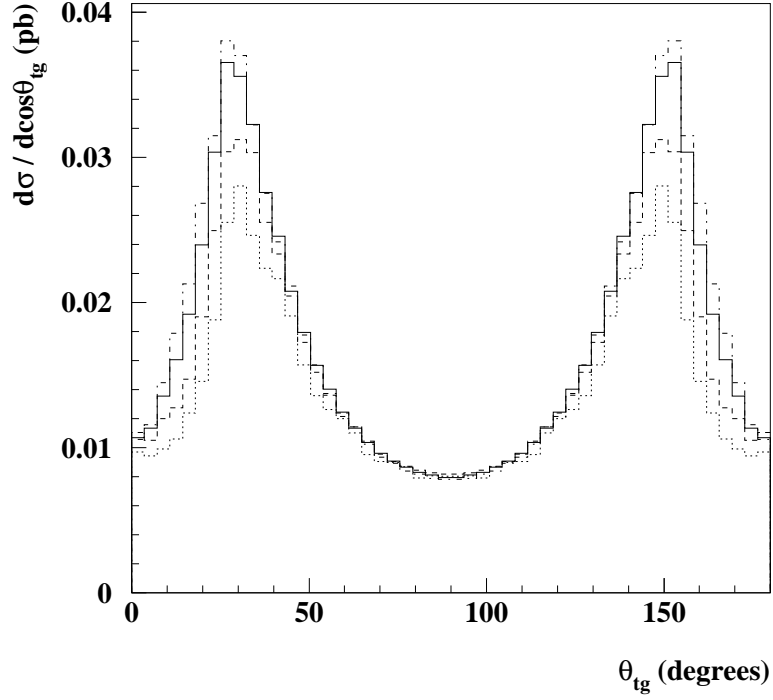


Figure 3-9: The distribution in angle between the top quark and the gluon for gluon energies from 5 to 10 GeV, $\cos \theta_{tb}, \cos \theta_{t\bar{b}} < 0.9$, and 750 GeV collision energy. The histograms correspond to different values of the top width Γ_t : dot-dashed: 0.1 GeV; solid: 1.42 GeV (SM); dashed: 5. GeV; dotted: 20 GeV.

$$f_{\bar{t}} > 0, \text{ if } \theta_{bg} > \theta_{\bar{b}g}, \quad (3.15)$$

we obtain the distribution shown in Figure 3-8. The interference effects are enhanced, though at the cost of a substantial decrease in cross section.

Because the production-decay interference is destructive, increasing the top width would further suppress the total distribution. The height of the peaks,

then, is sensitive to the value of Γ_t . This is illustrated in Figure 3-9, which shows the cross section (without the cuts of Eqs. 3.14,3.15) for different values of the top width⁵, ranging from 0.1 GeV to 20 GeV. The SM case ($\Gamma_t = 1.42$ GeV) is shown as a solid line. It is interesting to note that in the context of perturbative gluon radiation, the SM top width is actually a small quantity. There are several other points to note. In principle, this sensitivity to Γ_t gives us a method to measure the top quark's total width, independent of decay mode, above the top production threshold. Although in practice statistics would surely limit the possible precision of such a measurement, the total top width is not so easy to measure directly by any means. Furthermore, the effects illustrated here arise from simple quantum-mechanical interference, and finding experimental evidence for interference between the radiation at the various stages is an interesting goal by itself.

⁵The histograms here are scaled so that they all would have the same normalization in the absence of interference effects. Without this rescaling, changing the width while keeping the tbW coupling fixed changes the total cross section, which behaves like $1/\Gamma_t^2$ for small Γ_t .

Chapter 4

Virtual corrections

The subject of this chapter is the computation of virtual corrections to the process:

$$e^+e^- \rightarrow t \bar{t} \rightarrow b W^+ \bar{b} W^- \quad (4.1)$$

Although real gluon radiation plays an important role in top production and decay, the four particle final state in Eq. 4.1 will be the predominant signal observed experimentally. Therefore, it is of utmost interest to have good theoretical predictions for this process, and this means that the virtual corrections to the tree level amplitude should be computed.

While in studies of top quark production near threshold most of the information is extracted from the shape of the total cross section as a function of the beam energy, above threshold the information will be extracted from the analysis of kinematical variables of the decay products. Consequently, an analytic computation is much less useful in this case (and much less feasible, too), so the approach we will use to perform our computations will be Monte Carlo simulation.

One of the most important quantities to measure at future collider experiments is the top quark mass. A precise measurement of this parameter will allow stringent tests of the Standard Model of particle physics (or give information on

the supersymmetric model, if SUSY has been discovered by that time). Indeed, it is well known that, at the present time, the measured top quark mass together with values for the W boson mass and other electroweak parameters can be used to constrain the Higgs mass in the Standard Model (these constraints are not very strong so far, but they will be greatly enhanced by improvements in the top quark mass measurements [32]).

One way to measure the top mass at energies above the production threshold is by determining the position of the peak in the distribution of the invariant mass of the top decay products $\sqrt{(p_W + p_b)^2}$ (this is the way the top mass has been measured at the Tevatron). The quantity thus obtained is called the pole mass; the threshold studies will measure a quantity called the threshold mass (closely related to the $\bar{M}S$ mass)¹. A theoretical relation exists among these quantities; hence a measurement of both of them will allow a test of our understanding of the underlying theory.

The extraction of the top quark mass from the bW invariant mass distribution is the most natural and straightforward method; therefore, there are a lot of studies in this area (and we shall present some results of relevance to this case, too). However, it suffers from a fundamental limitation on the precision it can achieve: since the physical observable is not a color singlet, there will be uncertainties of order Λ_{QCD} in the measured quantities (what this actually means is that we cannot measure the momenta of the b jet - of any jet generated by a parton which has color, for that matter - with a precision greater than Λ_{QCD}). Therefore, the minimum error achievable through this method is about 200 MeV. In order to circumvent this limit, it might be desirable to try to extract the top mass from

¹Since a quark is not a stable particle, its mass is an elusive quantity; there are several theoretical definitions for the mass of the top quark; among these, the most common are the pole mass and the $\bar{M}S$ mass.

distributions which involve color singlet physical observables; for example, end points in distributions of quantities like $p_W(p_b + p_{\bar{b}})$, or the line shape of the decay leptons energies [7]. However, since these methods are quite involved, and would also require a good understanding of hadronization and detector issues, we will not discuss them further.

This kind of precision measurement obviously cannot be performed without a good theoretical understanding of the underlying process. Hence the need to compute the QCD corrections to the top production and decay process. A quick analysis shows that these corrections are indeed important. It is well known that the total NLO QCD corrections to the production of a pair of massless quarks is $\alpha_s/\pi \times$ the Born cross section. For the top production cross section, this would correspond to the high energy limit (beam energies of order TeV). On the other hand, near the top production threshold, the QCD corrections are quite large; from the results presented in [10], we have:

$$\sigma(e^+e^- \rightarrow t\bar{t}(g)) \longrightarrow \sigma^{\text{Born}} \left(1 + \alpha_s \frac{2\pi}{3\beta} \right), \quad \text{as } \beta \rightarrow 0$$

where β is the top quark speed ². This indicates that the NLO corrections to top production are rather large for CM energies smaller than 1 TeV; as we shall see below, they are about 20% of the Born cross section at 500 GeV, and 7% at 1 TeV.

In the following, we shall present a NLO computation for the top production and decay process which takes into account not only corrections to the production and decay subprocesses, but also interference contributions. The framework is

²Near the production threshold, fixed order NLO computation does not work anymore; rather, we need to perform a resummation of the large $\log\beta$ logarithms. Following the suggestion advanced in [10], we can assume that the NLO computation gives reasonable results if $\alpha_s/\beta < 1/4$, which means that the collision center-of-mass energy should be bigger than about 380 GeV.

that of the double pole approximation, as described in Chapter 2. The contributing amplitudes (Eq. 2.5) are computed using off-shell momenta, and numerical integrations for the cross section are performed over the full off-shell phase space. This approach allows for further development of our Monte Carlo (taking into account singly resonant terms, for example) to be performed in an easy and natural way. We shall also discuss an alternative computational method (on-shell DPA) and compare the results with those obtained in our approach. Some results on the total cross section for top production and decay and the impact of interference corrections on top mass reconstruction are presented at the end.

4.1 Resonant structure of partial amplitudes

In this section, we shall discuss the evaluation of NLO amplitudes contributing to the process 4.1. Some of the relevant Feynman diagrams are presented in Figure 2-4. As mentioned before, these diagrams can be split into two classes: (i) vertex and fermion self-energy diagrams, and (ii) interference diagrams. In the following, we shall look at each of these types separately, starting with the interference diagrams.

However, let's first consider some general properties of these amplitudes. In keeping with the approximation used (DPA), all of them have a doubly resonant behavior in the phase space region where the invariant mass of the Wb pair is close to the top mass. However, the exact type of behavior is different from diagram to diagram; while for the zero order amplitude the resonant behavior is of type *pole* \times *pole*:

$$\mathcal{M}_0 \sim \frac{1}{p_t^2 - \bar{m}_t^2} \frac{1}{p_t^2 - \bar{m}_t^2}$$

for the interference amplitudes the resonant behavior is formally of type *pole* \times

logarithm; for example:

$$\mathcal{M}_{b\bar{t}} \sim \log(p_t^2 - \bar{m}_t^2) \frac{1}{p_{\bar{t}}^2 - \bar{m}_t^2}$$

The replacement of a *pole*-type singularity with a *log*-type singularity can be traced back to the integration over the momentum of the gluon in the virtual loop. Moreover, this kind of term does not appear only in the purely interference diagrams, but also in the vertex and self-energy diagrams. The amplitude corresponding to the top decay vertex correction diagram, for example, can be written as a sum of terms:

$$\mathcal{M}_{tb} = \frac{1}{p_t^2 - \bar{m}_t^2} \frac{1}{p_{\bar{t}}^2 - \bar{m}_t^2} \tilde{\mathcal{M}}_{tdec} + \log(p_t^2 - \bar{m}_t^2) \frac{1}{p_{\bar{t}}^2 - \bar{m}_t^2} \mathcal{M}'_{tb}$$

where the terms with the double pole structure can be thought of as being the correction to the top decay process, and the term with a *pole* \times *log* structure contributes to interference between the production and top decay process.

Another property of the amplitudes for the interference diagrams is that, in the DPA, they are proportional to the tree level amplitude \mathcal{M}_0 . We say that, in the DPA, the interference amplitudes factorize. This is also true for the case of the W pair production process ([19], [21]); moreover, for this process it has been shown that *all* the interference contributions (including those coming from vertex correction diagrams, for example) factorize. Therefore, the total interference can be written as a scalar factor times the Born amplitude, which makes the evaluation of these contributions really easy. However, this is not true in our case; for the top production and decay process, there are interference contributions coming from the vertex and top self-energy correction diagrams which are not proportional to the tree level amplitude, as we shall see below.

4.1.1 Interference diagrams

In this section we will examine the behavior of interference diagrams. Consider, for example, the $\bar{t} - b$ interference diagram. (Fig. 2c). The amplitude associated with this diagram is:

$$\mathcal{M}_{b\bar{t}} = \bar{u}(b) \left[(-ig_s^2) \int \frac{d^4 k}{2\pi^4} \frac{1}{k^2 + i\epsilon} \gamma^\mu \frac{\not{p}_b - \not{k} + m_b}{(p_b - k)^2 - m_b^2} \not{\epsilon}_{W^+} \frac{\not{p}_t - \not{k} + m_t}{(p_t - k)^2 - \bar{m}_t^2} \Gamma_{\gamma, Z_0} \right. \\ \left. - \frac{\not{p}_{\bar{t}} - \not{k} + m_t}{(p_{\bar{t}} + k)^2 - \bar{m}_t^2} \gamma_\mu \right] \frac{-\not{p}_{\bar{t}} + m_t}{p_{\bar{t}}^2 - \bar{m}_t^2} \not{\epsilon}_{W^-} v(\bar{b}) \quad (4.2)$$

where the Feynman gauge is used for the gluon propagator.

The evaluation of this amplitude is obviously quite a difficult task. However, the only terms of interest to us in DPA are those which have resonances at the top and antitop quark propagator poles. This simplifies our task greatly. The doubly resonant terms can be extracted with the help of the following observation: if the virtual gluon in the loop is hard, then the quantity in brackets does not have any singularity, and the overall resonant structure for this diagram is given only by the pole due to the antitop propagator: $\mathcal{M}_{b\bar{t}}(\text{hard gluon}) \propto 1/(p_{\bar{t}}^2 - \bar{m}_t^2)$. This means that any doubly resonant terms contribution to $\mathcal{M}_{b\bar{t}}$ are entirely due to soft virtual gluons. Therefore, we can neglect the \not{k} terms in the numerator of (4.2). Following [19], we shall call this approximation the *extended soft gluon approximation* (ESGA) ³.

With the help of the transformations:

$$\gamma^\mu (\not{p}_b + m_b) = (-\not{p}_b + m_b) \gamma^\mu + 2p_b^\mu \rightarrow 2p_b^\mu \quad (4.3)$$

$$(-\not{p}_{\bar{t}} + m_t) \gamma_\mu = \gamma_\mu (\not{p}_{\bar{t}} + m_t) - 2p_{\bar{t}\mu} \rightarrow -2p_{\bar{t}\mu}$$

³In the standard soft gluon approximation, k^2 terms in the denominator of top quark propagators would also be neglected; we do not do this here for computational reasons (see also [28], [19]).

(the term $(\not{p}_{\bar{t}} + m_t)$ on the second line is neglected, since it would lead to a singly resonant contribution), the following result is obtained for the amplitude (4.2):

$$\mathcal{M}_{b\bar{t}}(DPA + ESGA) = \frac{\alpha_s}{4\pi} \mathcal{M}_0 * (-4p_b p_{\bar{t}})(p_t^2 - \bar{m}_t^2) * \int \frac{d^4 k}{i\pi^2} \frac{1}{k^2 + i\epsilon} \frac{1}{k^2 - 2k p_b} \frac{1}{(p_t - k)^2 - \bar{m}_t^2} \frac{1}{(p_{\bar{t}} + k)^2 - \bar{m}_t^2} \quad (4.4)$$

The result is proportional to the tree level amplitude – in the DPA, the virtual corrections due to interference factorize. The proportionality factor includes the scalar four point function (the integral on the second line of Eq. 4.4) $\mathcal{D}_{b\bar{t}}^0 = \mathcal{D}^0(-p_b, -p_t, p_{\bar{t}}, 0, m_b, \bar{m}_t, \bar{m}_t)$.⁴

What can we tell about the singular behavior of the DPA amplitude in (4.4)? Apparently, the result for $\mathcal{M}_{b\bar{t}}$ has a single pole at $p_t^2 = m_t^2$ (the other pole being canceled by the multiplicative term $p_t^2 - m_t^2$). However, if the top (or antitop) goes on-shell, the \mathcal{D}^0 function acquires an infrared singularity (in the zero top width limit; this singularity is regularized by the top width). Since the infrared singular type terms have a logarithmic structure (this can also be reasoned from power counting arguments), this indicates that \mathcal{D}^0 has the following behavior close to the top resonances:

$$\mathcal{D}_{b\bar{t}}^0 \sim a_1 \log(p_t^2 - \bar{m}_t^2) + a_2 \log(p_{\bar{t}}^2 - \bar{m}_t^2) \quad (4.5)$$

⁴ For the scalar one-loop integrals appearing here we use the following notation:

$$\mathcal{D}^0(p_1, p_2, p_3, m_0, m_1, m_2, m_3) = \int \frac{d^4 k}{i\pi^2} \frac{1}{N_0 N_1 N_2 N_3}$$

$$\mathcal{E}^0(p_1, p_2, p_3, p_4, m_0, m_1, m_2, m_3, m_4) = \int \frac{d^4 k}{i\pi^2} \frac{1}{N_0 N_1 N_2 N_3 N_4}$$

with the denominators :

$$N_0 = k^2 - m_0^2 + i\epsilon, \quad N_i = (k + p_i)^2 - m_i^2 + i\epsilon, \quad i = 1, \dots, 4$$

Here a_1 and a_2 are terms which are finite when *either* the top or antitop quark go on-shell.

Formally, then, the overall resonant behavior of the interference amplitude $\mathcal{M}_{b\bar{t}}$ in DPA is of type *pole* \times *logarithm*:

$$\mathcal{M}_{b\bar{t}} \sim \tilde{\mathcal{M}}_0 \log(p_t^2 - \bar{m}_t^2) \frac{1}{p_t^2 - \bar{m}_t^2}$$

rather than *pole* \times *pole*, as it is for the corrections to production or decay subprocesses.

Using the same techniques, similar results are easily obtained for the other two interference diagrams. In the soft gluon approximation (and DPA):

$$\mathcal{M}_{t\bar{b}}(DPA + ESGA) = \frac{\alpha_s C_F}{4\pi} \mathcal{M}_0 * (-4p_t p_{\bar{b}})(p_t^2 - \bar{m}_t^2) \mathcal{D}_{t\bar{b}}^0 \quad (4.6)$$

$$\mathcal{M}_{b\bar{b}}(DPA + ESGA) = \frac{\alpha_s C_F}{4\pi} \mathcal{M}_0 * (-4p_b p_{\bar{b}})(p_t^2 - \bar{m}_t^2)(p_t^2 - \bar{m}_t^2) \mathcal{E}_{b\bar{b}}^0 \quad (4.7)$$

where $\mathcal{D}_{t\bar{b}}^0 = \mathcal{D}^0(-p_{\bar{b}}, -p_{\bar{t}}, p_t, 0, m_b, \bar{m}_t, \bar{m}_t)$ and

$$\mathcal{E}_{b\bar{b}}^0 = \mathcal{E}^0(-p_b, -p_t, p_{\bar{t}}, p_{\bar{b}}, \mu, m_b, \bar{m}_t, \bar{m}_t, m_b) \quad (4.8)$$

is the scalar five point function (here μ is the infinitesimally small gluon mass needed for the regularization of infrared divergent behavior of $\mathcal{E}_{b\bar{b}}^0$).

We end this section with some comments on the numerical magnitude of interference terms. Since the resonant behavior of these terms is of *pole* \times *log* type, it might be expected that they are less important numerically than the double pole terms. However, analytic expressions for the \mathcal{D}_0 function ([19], [20], [21]) show that, although the coefficients a_1, a_2 in 4.5 are finite when one of the top or antitop quark goes on shell, they will diverge when both particles go on-shell simultaneously:

$$a_i \sim \frac{1}{c_{1i}(p_t^2 - \bar{m}_t^2) + c_{2i}(p_{\bar{t}}^2 - \bar{m}_t^2)}$$

Therefore, the leading logarithms in the scalar 4 and 5-point functions will be enhanced by factors of order m_t/Γ_t near the top, antitop quark mass resonances.

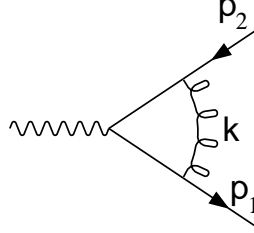


Figure 4-1: General vertex correction diagram.

4.1.2 Vertex corrections

The results for the interference diagrams are completely analogous to results obtained in the W pair production computation. However, for the off-shell vertex and self-energy corrections diagrams, the results in the top case are different. Consider for example, the amplitude for the general vertex correction in Figure 4-1:

$$\delta\Gamma^\mu = \frac{\alpha_s}{4\pi} \int \frac{d^4k}{i\pi^2} \frac{1}{k^2} \gamma^\nu \frac{\not{p}_1 - \not{k} + m_1}{(p_1 - k)^2 - \bar{m}_1^2} \gamma^\mu (C_V + C_A \gamma^5) \frac{-\not{p}_2 - \not{k} + m_2}{(p_2 + k)^2 - \bar{m}_2^2} \gamma_\nu$$

Upon evaluation (and keeping only the vector part) the result can be written in terms of eight form factors, each of them multiplying a different tensor quantity:

$$\delta\Gamma_V^\mu = \frac{\alpha_s}{4\pi} C_V [\gamma^\mu F_2 + (\not{p}_1 - m_1) \gamma^\mu F_4 + \gamma^\mu (-\not{p}_2 - m_2) F_6 + (\not{p}_1 - m_1) \gamma^\mu (-\not{p}_2 - m_2) F_8 + p_1^\mu F_1 + (\not{p}_1 - m_1) p_1^\mu F_3 + \dots] \quad (4.9)$$

(expressions for the scalar form factors F_1, \dots, F_8 can be found in the appendix). In the on-shell case, only the F_2 (electric dipole) and F_1 (magnetic dipole momentum) form factors contribute. It might be expected that in the double pole approximation we can drop the other terms, too, since they have a zero at $\not{p}_1 = m_1$ (or $\not{p}_2 = -m_2$) which will cancel one pole (or both) in the amplitude. However,

the form factors themselves may have a resonant structure when the particles go on shell.

Consider the top decay vertex correction. In this case, $p_1 \rightarrow p_b, p_2 \rightarrow -p_t$, and only four terms survive in Eq. 4.9; the corresponding form factors contain terms which are proportional to the scalar three point function:

$$F_i \sim C_{tb}^0 = \int \frac{d^4k}{i\pi^2} \frac{1}{k^2} \frac{1}{(p_b - k)^2 - m_b^2} \frac{1}{(p_t - k)^2 - \bar{m}_t^2} \quad i = 1, 2, 5, 6$$

which has a logarithmic resonant behavior:

$$C_{tb}^0 \sim \log(p_t^2 - \bar{m}_t^2).$$

Therefore, the contribution of $i = 5, 6$ terms to the top decay vertex correction is doubly resonant, although of type *pole* \times *log* rather than double pole. Because these logarithms are not multiplied by large factors (as in the case of the interference diagrams), we can expect these terms to be numerically small; for consistency reasons it is still desirable to include them in the final result.

Similar results are obtained for the correction to the antitop decay vertex (we keep the $i = 1, 2, 3, 4$ terms in this case). In the case of the $t - \bar{t}$ vertex, though, both fermions are off-shell; as a consequence, there are no resonant logarithms when either the top or antitop quark goes on-shell, and we keep only the $i = 1, 2$ terms.

It follows that in the general expression (4.9) we have to keep the terms which contain F_1 to F_6 (we can drop the F_7 and F_8 terms), and we don't have factorization anymore. This is different from what happens in the W pair production process, where in DPA factorization holds even in the off-shell case. This difference is due to the fact that in our process the intermediate particles are fermions, and not bosons.

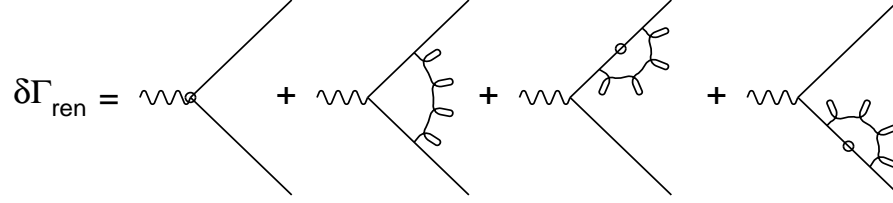


Figure 4-2: Terms contributing to the renormalized vertex; the dots represent counterterm insertions.

4.1.3 Renormalization and fermion self-energy

Since we are performing a next-to-leading order computation, we have to deal with the issue of ultraviolet divergences and renormalization. We use the counterterm method (for a presentation of the essential features see for example [23]). What renormalization amounts to in our case is replacing the bare vertex correction in Figure 4-1 (which is UV divergent) with a finite renormalized vertex correction:

$$\delta\Gamma^\mu \rightarrow \delta\Gamma_{ren}^\mu$$

$$\delta\Gamma_{ren}^\mu = \delta\Gamma^\mu + \Gamma^\mu \delta Z_2 + \frac{1}{2}(-i\hat{\Sigma}_2(\not{p}_1)) \frac{i}{\not{p}_1 - m_1} \Gamma^\mu + \frac{1}{2} \Gamma^\mu \frac{i}{-\not{p}_2 - m_2} (-i\hat{\Sigma}_2)(\not{p}_2) \quad (4.10)$$

in which we have included also the contributions of the fermion self-energy diagram. The diagrams corresponding to separate terms in Eq. 4.10 are presented in Figure 4-2.

The first two terms in Eq. 4.10 are what is usually defined as the renormalized vertex. The last two terms are one half of the renormalized fermion and antifermion self-energy:

$$\hat{\Sigma}_2(\not{p}) = \Sigma_2(\not{p}) - (\pm \not{p} - m)\delta Z_2 - \Delta m \quad (4.11)$$

where δZ_2 and Δm are coefficients of the counterterms in the Lagrangian den-

sity (the \pm sign corresponds to the particle/antiparticle case; one half because a fermion propagator connects to two vertices). In the above equation, Σ_2 stands for the *bare* fermion self-energy:

$$\Sigma_2(\not{p}) = \frac{\alpha_s}{4\pi} \int \frac{d^4k}{i\pi^2} \frac{1}{k^2} \gamma^\mu \frac{\not{p} - \not{k} + m}{(p-k)^2 - \bar{m}^2} \gamma_\mu \quad (4.12)$$

Upon evaluation, we can write the result for Eq. 4.12 in the form:

$$\Sigma(\not{p}) = (\pm \not{p} - m)\Sigma_a(p^2) + m\Sigma_b(p^2)$$

separating it into a scalar and a spinorial component. With these notations, the renormalized vertex correction can be written as:

$$\delta\Gamma_{ren}^\mu = \delta\Gamma^\mu + \frac{1}{2} \Delta Z_2(p_1) \Gamma^\mu + \frac{1}{2} \Gamma^\mu \Delta Z_2(p_2) \quad (4.13)$$

with

$$\Delta Z_2(p) = \Sigma_a(p^2) + \frac{m\Sigma_b(p^2) - \Delta m}{\pm \not{p} - m} \quad (4.14)$$

The counterterm coefficient Δm is fixed by the on-shell renormalization condition:

$$\hat{\Sigma}_2(\not{p} = m) = 0 \Rightarrow \Delta m = m\Sigma_b(m^2) \quad (4.15)$$

Also, in the on-shell limit,

$$\Delta Z_2(p)|_{\not{p} \rightarrow m} = \left(\Sigma_a(p^2) + \frac{\partial \Sigma_b(\not{p} \cdot \not{p})}{\partial \not{p}} \Big|_{\not{p} \rightarrow m} \right) = \frac{\partial \Sigma_2(\not{p})}{\partial \not{p}} \Big|_{\not{p} \rightarrow m} = \delta Z_2 \quad (4.16)$$

where for the last equality we have used the renormalization condition

$$\frac{\partial \hat{\Sigma}_2(\not{p})}{\partial \not{p}} \Big|_{\not{p} \rightarrow m} = 0$$

It is convenient to write the contribution of the fermion self-energy diagrams in a form similar to that of Eq. 4.9. Using the resummed top quark propagator:

$$\frac{i}{\pm \not{p} - m} \longrightarrow \frac{i(\pm \not{p} + m)}{p^2 - \bar{m}^2} \quad (4.17)$$

we obtain the following result for ΔZ_2 :

$$\Delta Z_2(p) = \left([\Sigma_a(p^2) + 2\Sigma_{ir}(p^2)] + \frac{\Sigma_{ir}(p^2)}{m}(\pm \not{p} - m) \right) \quad (4.18)$$

with

$$\Sigma_{ir}(p^2) = m \frac{\Sigma_b(p^2) - \Sigma_b(m^2)}{p^2 - \bar{m}^2}.$$

The term in square brackets in Eq. 4.18 will multiply the Born cross section. The term proportional to $(\pm \not{p} - m)$ is identical to the like terms appearing in the expression for the vertex correction Eq. 4.9. Since Σ_{ir} is the part of the self-energy correction which would be infrared divergent on-shell (which means that it has a logarithmic resonant behavior

$$\Sigma_{ir}(p^2) \sim \log(p^2 - \bar{m}^2)$$

in the off-shell case), we keep this term also.

4.2 Gauge invariance and corrections to particular subprocesses

The partial amplitudes appearing in Eq. (2.5) can be directly related to Feynman diagrams and are straightforward to evaluate. However, as mentioned before, they cannot be directly identified with corrections to particular subprocesses. For example, the top - antitop production vertex diagram (Figure 2-4a)) contributes to the correction to production vertex, as well as to interference between production and decay and even to interference between top decay and antitop decay, depending on when the top quark propagators are closer to the resonances. Moreover, the amplitudes in Eq. (2.5) are not gauge invariant one by one, although their sum is.

For purposes related to gauge invariance, and in order to be able to perform comparisons with the on-shell computation, it is desirable to decompose the total amplitude into gauge invariant corrections to particular subprocesses, and interference between these. The aim is to rewrite Eq. (2.5) as:

$$\mathcal{M}^{vg} = \mathcal{M}_{prod} + \mathcal{M}_{tdec} + \mathcal{M}_{\bar{t}dec} + \mathcal{M}_{prod-tdec}^{intf} + \mathcal{M}_{prod-\bar{t}dec}^{intf} + \mathcal{M}_{tdec-\bar{t}dec}^{intf} \quad (4.19)$$

with each term being gauge invariant by itself.

To this end, it is necessary to decompose the amplitudes $\mathcal{M}_{tt}, \mathcal{M}_{tb} \dots$ into parts which contribute solely to corrections to production, decay, or interference. This decomposition will be based on the top and antitop propagator structure of the matrix element. Following the prescription introduced in section 3.1.1, products of propagators which go on-shell in different regions of the phase space can be decomposed as follows:

$$\frac{1}{D(p_t)} \frac{1}{D(p_t - k)} = \frac{1}{D_0(p_t - k)} \frac{1}{D(p_t)} - \frac{1}{D_0(p_t - k)} \frac{1}{D(p_t - k)} \quad (4.20)$$

with

$$D(p) = p^2 - \bar{m}^2, \quad D_0(p - k) = (p - k)^2 - p^2 \quad (4.21)$$

In Eq. 4.20 the first term on the right hand side is considered as a contribution to the production process and the second one a contribution to the decay process. Furthermore, it is convenient to write the result in term of products of gauge invariant currents (in a manner similar to [19]). For example, the $\mathcal{M}_{b\bar{t}}$ amplitude can be written (using the extended soft gluon approximation):

$$\mathcal{M}_{b\bar{t}}(ESGA) = \frac{\alpha_s}{4\pi} \mathcal{M}_0 \int \frac{d^4 k}{i\pi^2} G_{\mu\nu}(k) \frac{-2p_t^\mu}{D(p_{\bar{t}} + k)} \frac{2p_b^\nu}{D_0(p_b - k)} \frac{D(p_t)}{D(p_t - k)} \quad (4.22)$$

where $G_{\mu\nu}(k)$ is the gluon propagator in an arbitrary gauge:

$$G_{\mu\nu}(k) = \frac{-i}{k^2 + i\epsilon} \left(g_{\mu\nu} - (\xi - 1) \frac{k_\mu k_\nu}{k^2} \right). \quad (4.23)$$

By using the currents :

$$j_{tdec}^{b, \mu} = \frac{2p_b^\mu}{D_0(p_b - k)} \frac{D(p_t)}{D(p_t - k)} \quad (4.24)$$

$$j_{prod}^{\bar{t}, \mu} = \frac{-2p_{\bar{t}}^\mu}{D_0(p_{\bar{t}} + k)} \quad , \quad j_{tdec}^{\bar{t}, \mu} = \frac{-2p_{\bar{t}}^\mu}{D_0(p_{\bar{t}} + k)} \frac{D(p_{\bar{t}})}{D(p_{\bar{t}} + k)}$$

we get :

$$\mathcal{M}_{b\bar{t}}(ESGA) = \frac{\alpha_s}{4\pi} \mathcal{M}_0 \int \frac{d^4k}{i\pi^2} G_{\mu\nu}(k) (j_{prod}^{\bar{t}, \mu} - j_{tdec}^{\bar{t}, \mu}) j_{tdec}^{b, \nu} \quad (4.25)$$

where the first term in parentheses contributes to production-decay interference, and the second one contributes to decay-decay interference.

We can similarly define the currents :

$$j_{tdec}^{\bar{b}, \mu} = \frac{-2p_b^\mu}{D_0(p_{\bar{b}} + k)} \frac{D(p_{\bar{t}})}{D(p_{\bar{t}} + k)} \quad (4.26)$$

$$j_{prod}^{t, \mu} = \frac{2p_t^\mu}{D_0(p_t - k)} \quad , \quad j_{tdec}^{t, \mu} = \frac{2p_t^\mu}{D_0(p_t - k)} \frac{D(p_t)}{D(p_t - k)}$$

and the amplitudes for the other two interference diagrams can be written like:

$$\mathcal{M}_{t\bar{b}}(ESGA) = \frac{\alpha_s}{4\pi} \mathcal{M}_0 \int \frac{d^4k}{i\pi^2} G_{\mu\nu}(k) (j_{prod}^{t, \mu} - j_{tdec}^{t, \mu}) j_{tdec}^{\bar{b}, \nu} \quad (4.27)$$

$$\mathcal{M}_{b\bar{b}}(ESGA) = \frac{\alpha_s}{4\pi} \mathcal{M}_0 \int \frac{d^4k}{i\pi^2} G_{\mu\nu}(k) j_{tdec}^{b, \mu} j_{tdec}^{\bar{b}, \nu} \quad (4.28)$$

Contributions to interference between subprocesses do not come solely from the manifestly non-factorizable diagrams. The diagrams in which the gluon contributes to vertex or self-energy corrections (Fig. 2a)) also contain interference terms. Since the decomposition into purely vertex (or self-energy) corrections and interference corrections is not unique, we shall present our approach in some detail.

The amplitude for the vertex correction diagram with off-shell particles can be written as :

$$(\delta\Gamma)_{12} = \frac{\alpha_s}{4\pi} \int \frac{d^4k}{i\pi^2} G_{\mu\nu}(k) \gamma^\nu \frac{A(p_1, p_2) + k^\alpha B_\alpha(p_1, p_2) + k^\alpha k^\beta C_{\alpha\beta}(p_1, p_2)}{((p_1 - k)^2 - m_1^2) ((p_2 + k)^2 - m_2^2)} \gamma_\nu \quad (4.29)$$

A corresponding on-shell approximation for this amplitude would be

$$(\delta\Gamma)_{os} = \frac{\alpha_s}{4\pi} \int \frac{d^4k}{i\pi^2} G_{\mu\nu}(k) \gamma^\nu \frac{A(p'_1, p'_2) + k^\alpha B_\alpha(p'_1, p'_2) + k^\alpha k^\beta C_{\alpha\beta}(p'_1, p'_2)}{(-2p'_1 k + k^2)(2p'_2 k + k^2)} \gamma_\nu \quad (4.30)$$

where p'_1 and p'_2 are some on-shell approximations for p_1 and p_2 . Now, we can define the interference contribution through:

$$(\delta\Gamma)_{12} = (\delta\Gamma)_{12}^{os} + (\delta\Gamma)_{12}^{intf} \quad (4.31)$$

Note, however, that $(\delta\Gamma)_{12}^{os}$ is not unique, since p'_1, p'_2 are not unique; different choices for these momenta would yield different results for $(\delta\Gamma)_{12}^{os}$. The uncertainty which arises is, of course, of order $p^2 - m^2$, so it can be neglected in the DPA. However, it allows us to choose the following definition for $(\delta\Gamma)_{12}^{os}$:

$$(\delta\Gamma)_{12}^{os} = \frac{\alpha_s}{4\pi} \int \frac{d^4k}{i\pi^2} G_{\mu\nu}(k) \left[\frac{(2p_1^\mu) \Gamma(-2p_2^\nu)}{D_0(p_1 - k)D_0(p_2 + k)} + \gamma^\mu \frac{k^\alpha B_\alpha(p_1, p_2) + k^\alpha k^\beta C_{\alpha\beta}(p_1, p_2)}{D(p_1 - k)D(p_2 + k)} \gamma^\nu \right] \quad (4.32)$$

This choice means that the purely vertex correction (factorizable) part of the vertex diagram can be obtained by simply replacing the off-shell $C_0(p_1, p_2, 0, m_1, m_2)$ function appearing in the expression for $(\delta\Gamma)_{12}$ with the on-shell, infrared divergent function $C_0(p_1, p_2, \mu, \sqrt{p_1^2}, \sqrt{p_2^2})$

Conversely, the interference part of the off-shell vertex correction diagram is:

$$(\delta\Gamma)_{12}^{intf} = \frac{\alpha_s}{4\pi} \int \frac{d^4k}{i\pi^2} G_{\mu\nu}(k) \left[\gamma^\mu \frac{A(p_1, p_2)}{D(p_1 - k)D(p_2 + k)} \gamma^\nu - \frac{(2p_1^\mu) \Gamma(-2p_2^\nu)}{D_0(p_1 - k)D_0(p_2 + k)} \right] \quad (4.33)$$

with $A(p_1, p_2) = (\not{p}_1 + m_1)\Gamma(-\not{p}_2 + m_2)$. For the $t\bar{t}$ production diagram, in DPA

$$\gamma^\mu (\not{p}_t + \bar{m}_t) \Gamma_{t\bar{t}}(-\not{p}_{\bar{t}} + \bar{m}_{\bar{t}}) \gamma^\nu \rightarrow (2p_t^\mu) \Gamma_{t\bar{t}}(-2p_{\bar{t}}^\nu)$$

leading to

$$\mathcal{M}_{t\bar{t}}^{intf} = \frac{\alpha_s}{4\pi} \mathcal{M}_0 \int \frac{d^4k}{i\pi^2} G_{\mu\nu}(k) \left[(-j_{tdec}^{t, \mu}) j_{prod}^{\bar{t}, \nu} + j_{prod}^{t, \mu} (-j_{tdec}^{\bar{t}, \mu}) + (-j_{tdec}^{t, \mu}) (-j_{tdec}^{\bar{t}, \mu}) \right] \quad (4.34)$$

Things are different for the decay vertices corrections, since we have doubly resonant contributions which are not proportional to the tree level matrix element. In the top decay case, the transformation:

$$\gamma^\mu (\not{p}_b + \bar{m}_b) \not{\epsilon}_{W^+} (\not{p}_t + \bar{m}_t) \gamma^\nu \rightarrow (2p_b^\mu) \not{\epsilon}_{W^+} [2p_t^\nu + \gamma^\nu (-\not{p}_t + \bar{m}_t)]$$

will lead to:

$$\mathcal{M}_{tb}^{intf} = \frac{\alpha_s}{4\pi} \int \frac{d^4 k}{i\pi^2} G_{\mu\nu}(k) j_{tdec}^{b, \mu} \left[(-j_{prod}^{t, \nu}) \mathcal{M}_0 + M_1^{t, \nu} \right] \quad (4.35)$$

where

$$M_1^{t, \mu} = \frac{-1}{D(p_t) D(p_{\bar{t}})} \left[\bar{u}(b) \not{\epsilon}_{W^+} \gamma^\mu \Gamma_{\gamma, Z_0} (-\not{p}_{\bar{t}} + \bar{m}_{\bar{t}}) \not{\epsilon}_{W^-} v(\bar{b}) \right] \quad (4.36)$$

In a similar manner, the interference term $\mathcal{M}_{t\bar{b}}^{intf}$ coming from the antitop vertex correction diagram can be written in terms of the currents $j_{tdec}^{\bar{b}, \mu}$, $-j_{prod}^{\bar{t}, \nu}$, and the matrix element $M_1^{\bar{t}, \nu}$.

Finally, the last diagrams to be split into on-shell and interference contribution are the top, antitop self-energy diagrams. Using the same approach as in the vertex case, we define:

$$\begin{aligned} (\Delta Z)_t^{intf} = & \frac{\alpha_s}{4\pi} \left\{ \int \frac{d^4 k}{i\pi^2} G_{\mu\nu}(k) \left[\gamma^\mu \frac{\not{p}_t + \bar{m}_t}{D(p_t - k)} \gamma^\nu - \frac{2p_t^\mu \gamma^\nu}{D_0(p_t - k)} \right] \right\} \frac{\not{p}_t + \bar{m}_t}{D(p_t)} - \\ & - \frac{\alpha_s}{4\pi} \int \frac{d^4 k}{i\pi^2} G_{\mu\nu}(k) \frac{2p_t^\mu}{D_0(p_t - k)} \frac{2p_t^\nu}{D_0(p_t - k)} (-1) \end{aligned} \quad (4.37)$$

where the quantity in the curly brackets is the renormalized top self-energy, and the quantity on the second line is the on-shell limit of the quantity on the first line. This will lead to the following result for the interference contribution coming from the top self-energy diagram:

$$\mathcal{M}_{tt}^{intf} = \frac{\alpha_s}{4\pi} \int \frac{d^4 k}{i\pi^2} G_{\mu\nu}(k) \left[j_{prod}^{t, \mu} \mathcal{M}_0 - M_1^{t, \mu} \right] j_{tdec}^{t, \nu} \quad (4.38)$$

and a similar one from the antitop self-energy diagram.

Now we have all the pieces needed to write down the interference terms. The final result is:

$$\begin{aligned} \mathcal{M}^{intf} = \frac{\alpha_s}{4\pi} \int \frac{d^4 k}{i\pi^2} G_{\mu\nu}(k) & \left[(j_{prod}^\mu \mathcal{M}_0 + M_1^{t, \mu}) j_{tdec}^\nu - (j_{prod}^\mu \mathcal{M}_0 - M_1^{\bar{t}, \mu}) j_{\bar{t}dec}^\nu \right. \\ & \left. + j_{tdec}^\mu j_{\bar{t}dec}^\nu \mathcal{M}_0 \right] \end{aligned} \quad (4.39)$$

It is easy in this formula to identify the production-decay or decay-decay interference terms. The currents:

$$j_{prod} = j_{prod}^{\bar{t}} - j_{prod}^t, \quad j_{tdec} = j_{tdec}^b - j_{tdec}^t, \quad j_{\bar{t}dec} = j_{\bar{t}dec}^{\bar{b}} - j_{\bar{t}dec}^{\bar{t}} \quad (4.40)$$

are conserved, and gauge invariant in DPA (that is, $k_\mu j^\mu = 0$, and the partial amplitudes in Eq. 4.39 are independent on the gauge parameter ξ in $G(k)$). Therefore, the total interference contribution as well as the interference between subprocesses parts are gauge invariant in the approximation used.

4.3 Computational Approach

Once a consistent scheme for evaluating the virtual corrections to the top production and decay process (4.1) has been set up (as described in the previous sections), the next step is the implementation of this scheme in a Monte Carlo program. In this section we give some details about the technical issues arising in the design of such a program, and how we choose to solve them.

There are two types of quantities involved in the evaluation of the NLO amplitude: scalar quantities (form factors), which encode the contribution of loops, and spinorial quantities, built from Dirac spinors and operators. For example, the contribution coming from the $t\bar{t}$ vertex correction can be written:

$$\tilde{\mathcal{M}}_{t\bar{t}} = \bar{u}(p_b) \not{\epsilon}_{W^+} (\not{p}_t + m_t) \delta\Gamma_{ren}^{t\bar{t}} (-\not{p}_{\bar{t}} + m_t) \not{\epsilon}_{W^-} v(p_{\bar{b}}) \quad (4.41)$$

or, using the decomposition in Eq. 4.9 :

$$\tilde{\mathcal{M}}_{t\bar{t}} = \frac{\alpha_s}{4\pi} \sum_{i=1,2} \left[C_V F_i^V T_i^V + C_A F_i^A T_i^A \right] \quad (4.42)$$

(definitions for the quantities appearing in the above equation can be found in Appendix **B**).

Let's start by discussing the evaluation of the scalar form factors F_i . Rather than compute analytic expressions for each form factor, we have chosen to evaluate them in terms of Passarino-Veltman (PV) functions [33]. This approach has the advantage that we have to compute only a few quantities which contain logarithms and dilogarithms: the \mathcal{B}_0 two-point and \mathcal{C}_0 three-point scalar functions (all the rest can be written as linear combination of these functions). In turn, for evaluating the PV 2 and 3-point scalar functions, we use the FF routines [34].

To compute the amplitudes corresponding to the interference diagrams, we need to be able to evaluate the 4-point and 5-point scalar integrals in Eqs. 4.4, 4.6, 4.7. There are no published results (or routines) for the general (complex masses) 4-point scalar integrals. We have build such routines for the infrared finite \mathcal{D}_0 function by using the general methods described in [35]. The results of these routines have been checked against analytical results in the soft gluon approximation published in [21].

The 5-point scalar function \mathcal{E}_0 has been computed by reduction to 4-point functions, following the recipe in [19]. The resulting infrared divergent 4-point functions have been evaluated using the analytic results published in [36].

Some comments on the treatment of the top width are needed here. One way of evaluating the scalar form factors in Eq. 4.42 is to compute the gluon integrals in the zero top width limit and introduce the finite width only in terms which are divergent on-shell (that is, replace m_t^2 with $\bar{m}_t^2 = m_t^2 - im_t\Gamma_t$ in terms like $\log(p_t^2 - m_t^2)$; see for example [19]). The difference between this result and the one

obtained by using the complex top mass in all the terms is of order Γ_t/m_t , therefore at about 1% level. This would be acceptable if the radiative corrections would be small with respect with the tree level result (as is the case for the W production process), but in our case it turns out that the one-loop QCD corrections are of the same order of magnitude as the tree level result ⁵. Therefore, order % terms are important. Since in the case of real gluon radiation the top width appears in all terms, for reasons of consistency we need to keep the width in all terms in the evaluation of the virtual corrections too.

The other elements needed in the evaluation of the amplitude (4.42) are the spinor sandwiches T_i . We compute these quantities using spinor techniques, as for the real gluon radiation case. Since this part of the computation is quite complex, and hence prone to errors, we have two different ways of performing it. In one approach, we express the T_i 's in terms of basic spinor products $\bar{u}(p_i, s_i)u(p_j, s_j)$; this is the more involved case (in terms of the work done by the programmer), geared for implementation in a Fortran routine, and which allows fast computation. The other approach uses C++ routines which allow the automated evaluation of general spinor sandwiches like

$$\bar{u}(p, s)(\not{p}_1 + m_1)(\not{p}_2 + m_2) \dots u(p', s')$$

(To this purpose, we have constructed classes that describe $\langle bra|$ and $|ket \rangle$ spinors, and operators of type $\not{p}_i \pm m_i$; in turn, these classes use the basic classes - 4-vector, complex number - defined in the Pandora event generator [37]). This method allows easy evaluation of T_i expressions (again from the programmer's viewpoint) and is much more resistant to programming errors; but the computation is slower than in the previous method. Therefore, the main use of the results

⁵the reason the *total* QCD corrections are of order 10 - 20% is because of large cancellations between the virtual corrections and soft gluon real corrections.

obtained from the C++ routines is to check the Fortran results.

4.4 On-shell DPA

The issue of interference effects in the production and decay of heavy unstable particles has been the subject of extensive studies in the past decade. Maybe the most important result is a theorem, due to Fadin, Khoze and Martin [38], which states that these interference effects are suppressed. A stronger version of this theorem [39] claims that NLO interference effects cancel in inclusive quantities up to terms of order $\alpha\Gamma/M$. Following the methods used in [39], it is possible to define a framework for the computation of interference corrections in which the total interference contribution to inclusive quantities is zero.

In this section we shall discuss this alternative approach (which we shall call on-shell DPA) to the computation of NLO corrections to the production and decay of unstable particles. Results obtained using this approach have been presented for the W pair production case at LEP II ([19], [21]); recently, this approach has been also applied in the computation of interference (non-factorizable) corrections to the top production and decay process at e^+e^- as well as at hadron colliders [40].

The relevant features of this approach are two: first, the amplitudes for corrections to subprocesses are computed in the on-shell approximation. For example, the correction to the production process can be written in terms of the on-shell amplitude:

$$\tilde{\mathcal{M}}_{prod}^{os} = \sum_{\lambda, \lambda'} \mathcal{M}_{\lambda, \lambda'}(e^+e^- \rightarrow t\bar{t}(g)) \mathcal{M}_{\lambda}(t \rightarrow bW^+) \mathcal{M}_{\lambda'}(\bar{t} \rightarrow \bar{b}W^-) \quad (4.43)$$

where λ, λ' are the spins of the top quarks. The difference between the above

amplitudes and the ones used in our computation (Eqs. 4.19, 3.6) is due to non-doubly resonant terms, therefore acceptable in DPA.

The other characteristic feature of the on-shell DPA method is that the interference due to real gluon radiation is computed by using a semianalytic approach. This approach rests on the observation that interference is due mainly to gluons of energies of order Γ_t ; therefore, we can use the (extended) soft gluon approximation in the evaluation of interference terms.

There are two stages where this approximation comes into play. First, we apply it at the matrix element evaluation level. For example, consider interference between the diagrams where the gluon is radiated from the bottom quark and from the antitop quark. Using the formulas in the Appendix B:

$$\begin{aligned} d\sigma_{tb}^{rg}(p_b, p_W, \dots, k) &\sim 2\text{Re} \left[\sum_{\epsilon_g} \mathcal{M}_b^{sg} (\mathcal{M}_t^{sg})^* \right] = \\ &= |\mathcal{M}_0(p_b, p_W, \dots)|^2 2\text{Re} \left[\frac{4p_{\bar{t}}p_b}{2kp_b + i\epsilon} \frac{p_t^2 - \bar{m}_t^2}{(p_t + k)^2 - \bar{m}_t^2} \frac{1}{(p_{\bar{t}} + k)^2 - \bar{m}_t^{2*}} \right]. \end{aligned} \quad (4.44)$$

The second stage is the treatment of the final state phase space. In the soft gluon approximation, we can factorize it: $d\Omega_{b,W,\dots,g} = d\Omega_{b,W,\dots} \times d\Omega_g$, and perform the integration over the gluon momenta analytically:

$$\begin{aligned} d\sigma_{tb}^{rg}(p'_b, p'_W, \dots) &= |\mathcal{M}_0(p'_b, p'_W, \dots)|^2 \times \\ &\frac{\alpha_s}{\pi} \text{Re} \left[\int \frac{d^3k}{2\pi\omega} \frac{4p_{\bar{t}}p_b}{2kp_b + i\epsilon} \frac{p_t^2 - \bar{m}_t^2}{(p_t + k)^2 - \bar{m}_t^2} \frac{1}{(p_{\bar{t}} + k)^2 - \bar{m}_t^{2*}} \right] \end{aligned} \quad (4.45)$$

where p'_b, p'_W, \dots are given by a suitable projection of the off-shell momenta p_b, p_W, \dots onto the on-shell phase space (for an example of how this projection might be accomplished see [41]). In the above equation we also have $p_t = p'_b + p'_{W+}$, $p_{\bar{t}} = p'_b + p'_{W-}$, and the integral over gluon momenta is allowed to go to infinity (since hard gluons contribute nonresonant terms to the result).

The quantity on the second line of Eq. 4.45 can be evaluated analytically, through methods similar to those used to evaluate the virtual 4-point functions. We will not give the results here (they can be found in [19], [21]), but there is an important comment to make. If we use this procedure to compute the real gluon interference, the total interference obtained by adding the virtual diagram contribution (Eq. 4.4) to the above result and integrating over the top invariant mass parameter is zero. The proof of this statement can be found in [39]. This cancellation works also for the other interference diagrams; therefore, in this approach, the contribution of non-factorizable corrections is zero to the total cross section. However, this result depends on two things. First, it requires an inclusive treatment of real gluon radiation, with phase space integration extending to infinity. Second, both the virtual and the real interference terms have to be treated in the soft gluon approximation.

But, is the use of the soft gluon approximation justified in this case? At the amplitude level (Eq. 4.44), the answer is yes; the relevant gluon energy, being of order Γ_t , is much smaller than the other momenta involved. However, this approximation does not seem to be acceptable for the phase space factorization stage of the above approach. Here, problems might arise when we try to perform the projection of the off-shell momenta onto the on-shell phase space. The reason for this is that there is no single way to perform this projection; therefore, in the determination of the on-shell momenta p'_b, p'_W, \dots there is an uncertainty of the order of the gluon energy, or Γ_t . Now, being close to the top resonances, we are in a region of the phase space where the cross section varies greatly over a range of energy of order Γ_t (due to the top quark propagators); therefore such an uncertainty is not acceptable.

To illustrate the dependence of the result for real gluon interference on the choice of the on-shell momenta p'_b, p'_W, \dots , let's presume that instead of projecting

p_b into p'_b , we also take into account the gluon momentum: $p_b + k \rightarrow p'_b$ (physically, this might be justified by the inclusion of the gluon jet in the bottom quark jet). Then, Eq. 4.45 becomes:

$$d\sigma_{tb}^{rg}(p'_b, p'_W, \dots) = |\mathcal{M}_0(p'_b, p'_W, \dots)|^2 \frac{\alpha_s}{\pi} \text{Re} \left[\int \frac{d^3k}{2\pi\omega} \frac{4p_{\bar{t}}p_b}{2kp_b + i\epsilon} \frac{1}{(p_{\bar{t}} + k)^2 - \bar{m}_t^{2*}} \right] \quad (4.46)$$

The result for the above expression is different from the result for Eq. 4.45, and the difference contains doubly resonant terms. Therefore, in the on-shell DPA approach, the result for the interference terms depends on how we perform the phase space factorization. A discussion of this dependence for the W pair production case can be found in [19].

4.5 Results for virtual corrections and the total cross section

In this section, we present some results on the total cross section for the top production and decay process at linear colliders. We take into account the virtual corrections as well as contributions coming from real gluon radiation. Furthermore, we study the effect of interference (nonfactorizable) terms on invariant top mass distributions and we perform comparisons with results previously published [40].

In obtaining the results presented in this section, the following set of parameters is used:

$$m_t = 175 \text{ GeV}, \quad \alpha_s = 0.1, \quad \Gamma_t^0 = 1.55 \text{ GeV}, \quad \Gamma_t = 1.42 \text{ GeV},$$

where Γ_t^0 is the top width at the tree level, while Γ_t includes QCD radiative corrections.

We start by looking at the total cross section for our process. Table 4.1 presents results for the following quantities:

- σ_0 : cross section for the tree level process (2.1); computed in the on-shell (narrow width) approximation, using the zero-order top width.
- σ_1^{os} : cross section for the NLO process in the on-shell approximation (computed using NLO top width).
- σ_1^{fact} : the main (factorizable) part of the DPA approximation to the NLO process. This quantity contains corrections to production and decay as defined in section 4.2.
- σ_1^{intf} : the interference (non-factorizable) part of the DPA approximation to the NLO process, as defined in section 4.2.

We present results for three values of collision center-of-mass energies: 360 GeV, just above the $t\bar{t}$ production threshold, 500 GeV, the most common value used in linear collider studies, and 1 TeV, which can be relevant for higher energy machines. Note that at 360 GeV our results are probably not good, being too close to the threshold; however, it is interesting to see the magnitude of the nonfactorizable corrections at fixed order in this energy range.

The NLO cross sections contain contributions from the virtual corrections as well as from real gluon radiation. We use a technical cut to separate the infrared from the real gluons $\epsilon = 0.1$ GeV; the results are independent of the choice of this parameter. No physical cuts have been imposed on the final phase space.

There are several comments to make concerning these results. First, let's compare σ_1^{os} with σ_1^{fact} . The difference between these two quantities is due to non-doubly-resonant terms, therefore it could be expected to be small. This is indeed the case at 500 GeV; but at 1 TeV, this difference is about 6% of the cross

	360 GeV	500 GeV	1000 GeV
σ_0	0.386	0.570	0.172
σ_1^{os}	0.700	0.660	0.184
σ_1^{fact}	0.676	0.664	0.197
σ_1^{intf}	-0.032	-0.012	-0.006

Table 4.1: Total cross sections for top production at linear colliders (measured in picobarns), with no cuts on phase space.

section. The reason is that in obtaining these results, we have integrated over the complete kinematic range available for the top quark invariant mass (that is, $m_b + m_W < \sqrt{p_t^2} < W - (m_b + m_W)$), so we get contributions from regions of the phase space where the top quarks are far off-shell and non-resonant terms are important.

In Table 4.2 we present the cross section results obtained with a cut on the t, \bar{t} invariant mass $|\sqrt{p_t^2}, \sqrt{p_t^2} - m_t| < 15$ GeV. The difference between the two results for the main terms σ_1^{os} and σ_1^{fact} is small in this case. Note that, since in the on-shell approach $p_t^2, p_{\bar{t}}^2 = m_t^2$, σ_1^{os} in Table 4.1 and 4.2 contains a factor which simulates the effect of cuts (either from kinematic constraints or imposed ones)

	360 GeV	500 GeV	1000 GeV
σ_1^{os}	0.682	0.627	0.175
σ_1^{fact}	0.670	0.629	0.178
σ_1^{intf}	-0.034	-0.007	-0.002

Table 4.2: Total cross sections for top production at linear colliders (measured in picobarns), with cuts on the top, antitop invariant mass.

on the top invariant mass. Note also that these cuts are not imposed *ad hoc*, but they arise rather naturally in the process of defining a t, \bar{t} production event; it makes sense to require that the reconstructed mass of the b, W pairs is close to the top mass in the definition of such an event. In this context, it is also worth noting that the contribution coming from the phase space region where either the t or \bar{t} is far off-shell (more than ten times the width) is quite sizable (around 5% of the total cross section for CM energies greater than 500 GeV).

Another quantity of interest is the differential interference cross section as a function of the top invariant mass. Even if the total interference contribution to the cross section is small (at about 1% level), it can have larger effects in differential distributions since it can be positive in certain regions of the phase space and negative in others. In particular, it can be important in the reconstruction

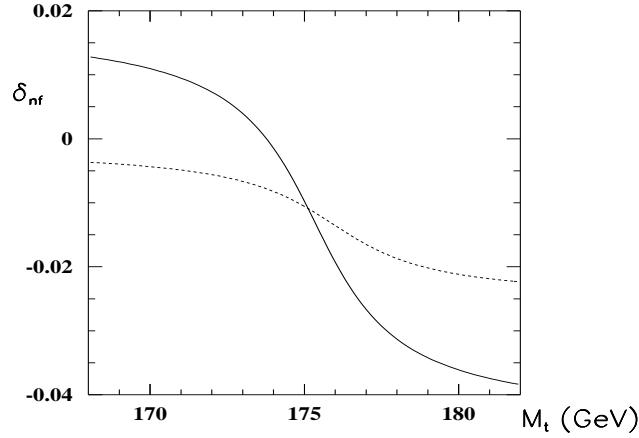


Figure 4-3: The relative nonfactorizable correction to the invariant mass distribution; the solid line is the contribution of terms proportional to the tree level amplitude, while the dashed line contains also the M_1 terms in Eq. 4.39.

of the top invariant mass; since $d\sigma_1^{intf}$ tends to decrease as $\sqrt{p_t^2}$ increases, the net effect would be to shift the position of the Breit-Wigner peak to smaller invariant mass values. This effect can be quantified by the following equation: the shift in the mass is

$$\Delta M_t = \left(\frac{d\delta_{nf}}{dM_t} \right) \Big|_{M_t=m_t} \frac{\Gamma_t^2}{8} \quad (4.47)$$

where $M_t = \sqrt{p_t^2}$, and δ_{nf} is the ratio of the non-factorizable (interference) part of the cross section to the Born cross section:

$$\delta_{nf} = \frac{d\sigma_1^{intf}}{d\sigma_0}$$

In Figure 4-3 we present the differential distribution for the relative non-factorizable correction $\delta_{nf}(M_t)$ at center of mass energy 500 GeV. The dashed line is the result which takes into account the full interference corrections in Eq. 4.39; the solid line is obtained by taking into account only the terms proportional to the Born amplitude. Note that, although the contribution of the M_1 terms in

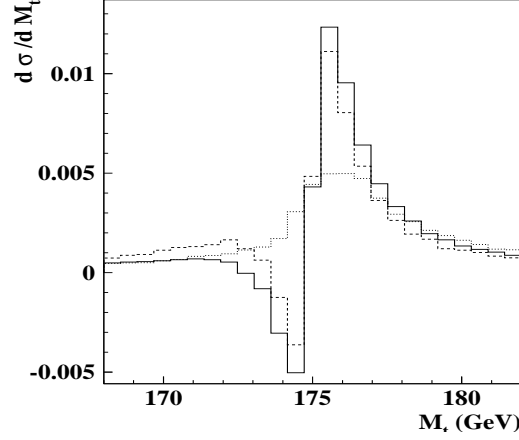


Figure 4-4: Real gluon interference: the $\sigma_{b\bar{t}}$ term. The solid line corresponds to the semianalytic approach; the dashed line is obtained through numerical evaluation with $M_t = \sqrt{p_{bW}^2}$; the dotted line is obtained through numerical evaluation with M_t given by Eq. 4.48.

Eq. 4.39 to the total cross section is very close to zero, they have a sizable effect on the differential distribution in Fig. 4-3. Using Eq. 4.47, we conclude that the shift in the position of the peak in the top invariant mass distribution due to interference effects is very small (of order of a few MeV).

The results in Table 4.1 and 4.2 indicate that the contribution of interference terms to the total cross section is of order 1%, in agreement with the Γ_t/m_t order of magnitude expected from naive arguments. However, it is not zero, as implied by results presented in [40], which use the on-shell DPA method. We have argued in section 4.4 that this difference is due to the way in which the radiation of real gluon with energies of order Γ_t is treated. In Figure 4-4, we present the results for the real interference between the diagram where the gluon is radiated from the bottom quark and the diagram where the gluon is radiated from the antitop quark. The solid line is the result of the semianalytical approach described in

section 4.4. The other two lines are the result of the exact off-shell computation (where the integration over the gluon momenta is performed numerically). The two lines correspond to two different ways in which the gluon momentum is treated in the reconstruction of the invariant top mass. For the dashed line, the gluon momentum is ignored in the top mass reconstruction: $M_t = \sqrt{p_{bW}^2}$. Note that in this case, the result is quite close to that of the semianalytical computation, which is natural, since the gluon momentum is treated in both cases the same way.

To obtain the dotted line, we have followed a more realistic approach, in which the gluon is included in the top mass reconstruction if it happens to be radiated close enough to the top quark:

$$M_t = \begin{cases} \sqrt{p_{bWg}^2} & \text{if } \cos\theta_{tg} < \pi/3 \\ \sqrt{p_{bW}^2} & \text{otherwise} \end{cases} \quad (4.48)$$

Although the total cross section is the same as for the other exact evaluation case, the differential cross section differs by quite a bit.

The total cross section corresponding to the interference term presented in Figure 4-4 has the value $\sigma_{b\bar{t}} = 0.121 \text{ pb}$ for the semianalytical result, and $\sigma_{b\bar{t}} = 0.124 \text{ pb}$ for the numerical one. Note that, since the diagram set contributing to this interference term is not gauge invariant, this result has no physical meaning by itself. However, from these numbers we can get some insight concerning the evaluation of interference corrections. First, note that the contribution of this single diagram is much bigger (about two orders of magnitude) than the total result for the interference terms. This means that there are large cancellations taking place between the real and virtual interference contributions. This is quite natural, in accordance with the discussion in section 4.4; however, this also means that small uncertainty (order percent) in evaluating one of this contributions (the one coming from the real gluon interference, for example) can lead to large uncertainties

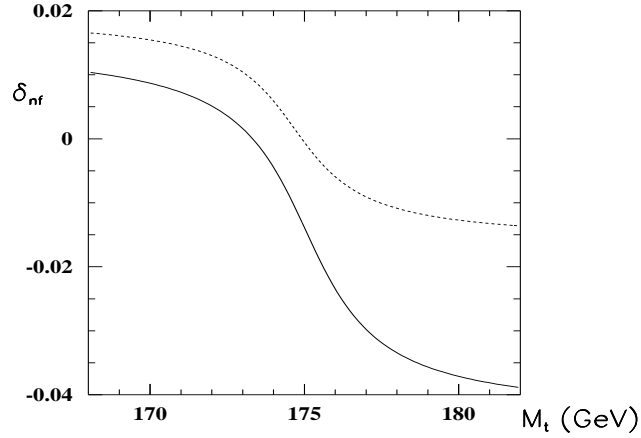


Figure 4-5: The relative nonfactorizable correction to the invariant mass distribution; comparison between the semianalytical (dashed line) and the numerical (solid line) approach.

in the evaluation of the total interference contribution.

In Figure 4-5 we present the comparison between the relative non-factorizable corrections computed in the semianalytical approximation (dashed line) and the complete off-shell approach (solid line). For the purpose of this comparison, we consider only the terms proportional to the Born amplitude in the exact computation, since only these terms are taken into account in the semianalytical approach. Note that the total interference cross section integrates to zero in the latter case, and, as discussed above, the complete off-shell distribution contains contributions that do not cancel in the total cross section.

Chapter 5

Conclusions

In this thesis, we have discussed in some detail the evaluation of next to leading order QCD corrections to the top production and decay process at a linear collider. Since a full computation of the NLO amplitudes contributing to the process $e^+e^- \rightarrow b W^+ \bar{b} W^-$ is not feasible, we have employed the double pole approximation. In our case this means taking into account only the diagrams which contain two intermediate top quarks. Unlike most of the previous treatments, we allow for the two top quarks to be off-shell, and include also the corrections due to interference between the top production and decay processes.

This thesis can be roughly split into two parts: the first one deals with the radiation of a real gluon in top production and decay, and the second one deals with the computation of virtual corrections and the radiation of soft gluons in this process. For the real gluon radiation case, we give a method to split the contributing amplitudes into parts which can be thought of as associated with the top production or decay subprocesses. This allows for the separation of the cross section into parts describing gluon radiation in top production, top decay, and interference. We discuss the properties of the gluon radiation, and analyze the

impact the gluon has on top mass reconstruction. We pay special attention to the analysis of interference terms; since the magnitude of these terms depends on the top width, they might provide a way to measure this quantity at energies above the threshold. Even if this is not possible, observing experimental evidence for interference between the radiation at various stage is an interesting goal by itself. Although further studies are needed, our analysis indicates that, while difficult, this goal is not *a priori* unreachable.

For the virtual gluon corrections case, we first discuss the evaluation of contributing amplitudes in the double pole approximation. A parallel is drawn between our computation and the DPA evaluation of QED corrections to the W pair production and decay process at LEP. While there are many similarities between the two computations, there are also some differences; maybe the most important one is that there are nonfactorizable (interference) corrections no longer proportional to the Born amplitude in the top quark case. Previous analyses state that the interference terms cancel out completely in inclusive quantities (like the total cross section). We discuss the evaluation of the real gluon interference terms using analytic methods and we point out the shortcomings of this approach. The total magnitude of nonfactorizable corrections in our computation is found to be of order 1% of the cross section. We also present results for the total cross section and the relative nonfactorizable correction to the top invariant mass distribution. The effect of nonfactorizable corrections on the top mass reconstruction is found to be very small.

The computations in this thesis are valid at collision energies above the top-antitop production threshold. Since we are interested in differential distributions of final state kinematic variables, the approach used to obtain the results presented throughout the paper is that of numerical simulations. The amplitudes are evaluated using spinor techniques, and the integration over the final state variables is

performed using Monte Carlo techniques. This approach has the added advantage that it allows for the inclusion of experimentally relevant selection criteria on the final state phase space.

The calculation presented here is entirely at the parton level. For more realistic simulations, it is necessary to take into account initial state related issues, like initial state radiation (ISR), beam energy spread and beamstrahlung. The hadronization of the final state partons also has to be modeled. In order to address these issues, we plan to provide an interface of our code with Pandora (a general physics event generator for linear collider studies which includes ISR and beamstrahlung effects) and Pythia (a Monte Carlo which simulates final state parton shower and hadronization).

For the future, we plan to extend our computations by including all the lowest order diagrams contributing to our process. Also, the evaluation of NLO corrections to the singly resonant diagrams in the on-shell approximation should prove feasible. Beyond QCD, we plan to take into account electroweak radiative corrections to the top production and decay process, and maybe SUSY corrections too. The framework we use for our computations is flexible enough to build on the results presented in this thesis with the final goal of constructing a comprehensive Monte Carlo for top related issues at future linear colliders.

Bibliography

- [1] E. Fahri and L. Susskind, Phys. Rept. **74** (1981) 277
- [2] for a review see, e.g., H. E. Haber and G.L. Kane, Phys. Rept. **117** (1985) 75
- [3] I.I. Bigi et al., Y.L. Dokshitzer, V. Khoze, J. Kuhn and P. Zerwas, Phys. Lett. **B181** (1986) 157; L.H. Orr and J.L. Rosner, Phys. Lett. **B246** (1990) 221 , **248** (1990) 474(E); L.H. Orr, Phys. Rev. **D44** (1991) 88
- [4] F. Abe et al., CDF Collaboration, Phys. Rev. Lett. **74** (1995) 2626, S. Abachi et al., D0 Collaboration, Phys. Rev. Lett. **74** (1995) 2632
- [5] The Top Averaging Group, CDF and D0 Collaborations, Fermilab-TM-2084 (1999)
- [6] Top Quark Physics, M.Beneke et al., contribution to the '1999 CERN Workshop on SM physics (and more) at the LHC', CERN-TH/2000-102, hep-ph/0003033
- [7] T. Abe et al., [American Linear Collider Working Group Collaboration], *Resource book for Snowmass 2001, 30 Jun - 21 Jul 2001, Snowmass, Colorado* SLAC-570, hep-ex/0106057, hep-ex/0106058

- [8] B. Grzadkowski and Z. Hioki, Nucl. Phys. **B585** (2000) 3, Phys. Rev. **D 61** (2000) 014013, and Phys. Lett. **B476** (2000) 87
- [9] A. H. Hoang et al., Eur. Phys. J. Direct **C3** (2000) 1, and references therein
- [10] J. Jersak, E. Laerman, and P. Zerwas, Phys. Rev. **D 25** (1982) 1218
- [11] J.G.Korner, A.Pilaftsis, and M.M. Tung, Z. Phys. C **63** (1994) 575
- [12] J. Kodaira, T. Nasuno, and S. Parke, Phys. Rev. **D 59** (1999) 014023
- [13] A. Brandenburg, M. Flesch, and P. Uwer, Phys. Rev. **D 59** (1999) 014001
- [14] M. Jezabeck and J.H. Kuhn, Nucl. Phys. **B314** (1989) 1
- [15] A. Czarnecky, Phys. Lett. **B252** (1990) 467
- [16] C.S. Li, R.J. Oakes, and T.C. Yuan, Phys. Rev. **D 43** (1991) 3579
- [17] C. R. Schmidt, Phys. Rev. **D 54** (1996) 3250
- [18] A. Denner, S. Dittmaier, M. Roth and D. Wackeroth, Nucl. Phys. **B560** (1999) and Nucl. Phys. **B587** (2000) 67
- [19] A. Denner, S. Dittmaier, and M. Roth, Nucl. Phys. **B519** (1998) 39
- [20] K. Melnikov and O. I. Yakovlev, Nucl. Phys. **B471** (1996) 90
- [21] W. Beenakker, F. A. Berends, and A. P. Chapovsky, Phys. Lett. **B411** (1997) 203 and Nucl. Phys. **B508** (1997) 17
- [22] T. Stelzer and W. F. Long, Comp. Phys. Comm. **81** (1994) 357
- [23] M. E. Peskin and D. V. Schroeder, *An Introduction to Quantum Field Theory*, Addison-Wesley Publishing Company, 1995

- [24] F. Bloch and A. Nordsieck, Phys. Rev. **52** (1937) 54
- [25] D. Yennie, S. Frautschi and H. Suura, Ann. Phys. **13** (1961) 379
- [26] U. Baur and D. Zeppenfeld, Phys. Rev. Lett. **75** (1995) 1002, E. N. Argyres et al., Phys. Lett. **B358** (1995) 339, W. Beenakker et al., Nucl. Phys. **B500** (1997) 255 and references therein
- [27] G. Jikia, Phys. Lett. **257B** (1991) 196.
- [28] V.A. Khoze, L.H. Orr, and W.J. Stirling, Nucl. Phys. **B378** (1992) 413
- [29] C. Macesanu and L. H. Orr, submitted to Phys. Rev. **D**, hep-ph/0012177
- [30] R. Kleiss and W. J. Stirling, Nucl. Phys. **B262** (1985) 235
- [31] G. Siopsis, Phys. Rev. **D58**, 014009 (1998).
- [32] D. Abbaneo et al., [ALEPH, DELPHI, L3 and OPAL Collaborations, LEP Electroweak Working Group, and SLD Heavy Flavour and Electroweak Groups], CERN-EP/2001-021, hep-ex/0103048
- [33] G. Passarino and M. Veltman, Nucl. Phys. **B160** (1979) 151
- [34] G.J. van Oldenborgh, Comp. Phys. Comm. **66** (1991) 1-15
- [35] G. 't Hooft and M. Veltman, Nucl. Phys. **B153** (1979) 365.
- [36] W. Beenakker and A. Denner, Nucl. Phys. **B338** (1990) 349
- [37] M.E. Peskin, SLAC-PUB-8290, hep-ph/9910519
- [38] V.S. Fadin, V.A. Khoze and A.D. Martin, Phys. Lett. **B320** (1994) 141
- [39] V.S. Fadin, V.A. Khoze and A.D. Martin, Phys. Rev. **D 49** (1994) 2247

- [40] W. Beenakker, F. A. Berends, and A. P. Chapovsky, Phys. Lett. **B454** (1999) 129
- [41] W. Beenakker, F. A. Berends, and A. P. Chapovsky, Nucl. Phys. **B548** (1999) 3
- [42] CALKUL Collaboration, Phys. Lett. **B105** (1981) 215, **B114** (1982) 203; Nucl. Phys. **B206** (1982) 53, **B206** (1982) 61, **B239** (1984) 382, **B239** (1984) 395

Appendix A

Spinor techniques

The standard technique for computing a cross section used to rely on the evaluation of the square of the amplitude with the help of trace formulas. More recently, since the complexity of the processes being analyzed has increased, this approach has proven to be too cumbersome. To understand why this is so, note that if the total amplitude gets N contributions from N different Feynman diagrams, the evaluation of the square amplitude through trace techniques requires the computation of N^2 terms. Thus, in recent years the emphasis has shifted toward the evaluation at the amplitude level, using spinor techniques.

These techniques have been developed by a number of people over a number of years (for some examples, see [42]). We will use the particular scheme proposed by Kleiss and Stirling in [30]; for the sake of completeness, we review here the general features.

A.1 Spinors describing massive and massless fermions

A spinor describing a massless particle of momentum p and helicity λ can be constructed with the help of two auxiliary 4-vectors k_0 and k_1 and the basic spinor $u_-(k_0)$:

$$u_\lambda(p) = \frac{\not{p}}{\sqrt{2p k_0}} u_{-\lambda}(k_0) \quad (\text{A.1})$$

The k_0 and k_1 vectors have to satisfy the following conditions :

$$k_0 k_0 = 0, \quad k_1 k_1 = -1, \quad k_0 k_1 = 0 \quad (\text{A.2})$$

k_1 is necessary in order to define the relative complex phase of the positive helicity k_0 spinor in relation to the negative one : $u_+(k_0) = \not{k}_1 u_-(k_0)$.

The basic elements from which the total amplitude can be ultimately constructed are the products of two massless spinors:

$$\bar{u}_{\lambda_1}(p_1) u_{\lambda_2}(p_2)$$

These basic spinor products can be expressed in terms of a single complex function $s(p_1, p_2)$:

$$\bar{u}_+(p_1) u_-(p_2) = s(p_1, p_2) \quad (\text{A.3})$$

$$\bar{u}_-(p_1) u_+(p_2) = t(p_1, p_2) = [s(p_2, p_1)]^*$$

$$\bar{u}_\lambda(p_1) u_\lambda(p_2) = 0$$

The exact form of function $s(p_1, p_2)$ depends on the choice for the auxiliary vectors k_0 and k_1 . Using the values suggested in [30]:

$$k_0 = (1, 1, 0, 0), \quad k_1 = (0, 0, 1, 0) \quad (\text{A.4})$$

we have :

$$s(p_1, p_2) = (p_1^y - ip_1^z) \frac{\eta(p_2)}{\eta(p_1)} - (p_2^y - ip_2^z) \frac{\eta(p_1)}{\eta(p_2)}, \quad \text{with } \eta(p) = \sqrt{2pk_0} \quad (\text{A.5})$$

The spinor which describes a massive fermion of momentum q can be similarly defined, with an added degree of complexity: since the number of inner degrees of freedom is four for a massive fermion as opposed to two for a massless one, we have an extra degree of freedom in our definition:

$$u(q, s) = \frac{1}{m} (\not{p}_1 + \not{p}_2 \pm m) u_{\pm}(p_2) \quad (\text{A.6})$$

(the minus sign in the parentheses above corresponds to the antiparticle case) where p_1 and p_2 are any two momenta which satisfy the constraints:

$$p_1^2 = p_2^2 = 0, \quad p_1 + p_2 = q. \quad (\text{A.7})$$

What this extra freedom amounts to is the liberty to choose along which axis the spin of the fermion points. It can be shown that the spin vector is given by

$$s = (p_1 - p_2)/m. \quad (\text{A.8})$$

An appropriate choice for the vectors p_1, p_2 will allow decomposition in the helicity basis, for example. However, since in our case we are not interested in specific spin states for the massive fermions (the spin of the b quarks is not observable, and the top quark is off-shell), we have chosen a definition which, while not particularly relevant physically, it is computationally convenient:

$$p_1 = q - \frac{m^2}{2qk_0} k_0, \quad p_2 = \frac{m^2}{2qk_0} k_0 \quad (\text{A.9})$$

Now, since $\not{k}_0 u(k_0) = 0$ and $u(\alpha k_0) = \sqrt{\alpha} u(k_0)$ (from normalization constraints), we get:

$$u(q, \pm s) = \frac{\not{q} + m}{\sqrt{2qk_0}} u_{\mp}(k_0), \quad v(q, \pm s) = \frac{\not{q} - m}{\sqrt{2qk_0}} u_{\pm}(k_0) \quad (\text{A.10})$$

$$\text{with} \quad s = \frac{q}{m} - \frac{m}{qk_0}k_0$$

(note that for the antiparticle spinor, the sign of the spin is reversed, as it should be, since in the massless limit, the antiparticle is identical to the particle of opposite helicity).

With these definitions, we get the following expressions for the massive spinor products:

$$\begin{aligned} \bar{u}_+(q_1)u_-(q_2) &= s(q_1, q_2), \quad \bar{u}_-(q_1)u_+(q_2) = t(q_1, q_2) \\ \bar{u}_+(q_1)u_+(q_2) &= \bar{u}_-(q_1)u_-(q_2) = m_1 \frac{\eta(q_2)}{\eta(q_1)} + m_2 \frac{\eta(q_1)}{\eta(q_2)} \end{aligned} \quad (\text{A.11})$$

with the s and t functions the same as in Eqs. A.3, A.5. If one spinor represents an antiparticle, the corresponding mass changes sign in the second line of the equation above.

The total amplitude can be written in term of the basic spinor products discussed above. Terms like

$$\bar{u}(p_1) \not{p}_i \not{p}_j \dots u(p_2)$$

are evaluated using the completeness relations

$$\sum_{\lambda} u(p)\bar{u}(p) = \not{p} + m, \quad \sum_{\lambda} v(p)\bar{v}(p) = \not{p} - m \quad (\text{A.12})$$

while terms of the form:

$$[\bar{u}_{\lambda_1}(p_1)\gamma^\mu u_{\lambda_2}(p_2)][\bar{u}_{\lambda_3}(p_3)\gamma_\mu u_{\lambda_4}(p_4)]$$

can be evaluated using the Chisholm identity; for massless spinors:

$$\bar{u}_{\lambda_1}(p_1)\gamma^\mu u_{\lambda_2}(p_2)\gamma_\mu = \begin{cases} 2 [u_{\lambda}(p_2)\bar{u}_{\lambda}(p_1) + u_{-\lambda}(p_1)\bar{u}_{-\lambda}(p_2)] & \text{if } \lambda_1 = \lambda_2 = \lambda \\ 0 & \text{if } \lambda_1 \neq \lambda_2 \end{cases} \quad (\text{A.13})$$

A.2 Spinors describing massless bosons

The only massless external boson contributing to our process is the gluon. The polarization vector for the gluon can be built with the help of an auxiliary vector k_a :

$$\epsilon^\mu_\lambda = \frac{1}{\sqrt{4kk_a}} \bar{u}_\lambda(k) \gamma^\mu u_\lambda(k_a) . \quad (\text{A.14})$$

Here, λ stands for the helicity of the gluon (+ or -); we take into account only states of physical, transverse polarization. The freedom given by the possibility to choose k_a corresponds to freedom in the choice of the gluon gauge.

In relation to the gluon gauge choice, it is worth mentioning here an important point concerning numerical instabilities. When the gluon momentum and the auxiliary vector for the gluon gauge are almost parallel ($kk_a \approx 0$), the normalization factor in Eq. A.14 will become very large. If the total amplitude is gauge invariant, this is of no concern (besides the fact that there will be large cancellations between different terms in the amplitude). However, if the total amplitude contains terms which are not gauge invariant, even if they are usually small, these terms will be enhanced. In other words, the cancellations between large terms won't be exact anymore. Obviously this is a problem; the solution is either to use a completely gauge invariant amplitude in our computation, or make sure that the auxiliary vector k_a points in different direction from the gluon momentum.

A.3 Spinors describing massive bosons

The treatment of massive boson (W) polarization states actually amounts to letting the W decay into two massless particles (an electron and an antineutrino, for example) and integrating over the momenta of these particles. The sum over

polarizations can be evaluated as follows:

$$\sum_{\epsilon} \epsilon^{\mu} \epsilon^{*\nu} \rightarrow \frac{3}{8\pi m^2} \int d\Omega a^{\mu} a^{*\nu} \quad ; \quad a^{\mu} = \bar{u}_{-}(r_1) \gamma^{\mu} u_{-}(r_2) \quad (\text{A.15})$$

r_1 and r_2 being two lightlike vectors (the momenta of the two massless particles) which add up to the momentum of the massive boson, and the integral is over the direction of r_1 .

In our computation, the polarization vector for the W boson stands for:

$$\epsilon_W = \left(\frac{-ig_W}{\sqrt{2}} \gamma^{\mu} P_L \right) \frac{-i}{p_W^2 - M_W^2 + iM_W \Gamma_W} \left[\bar{u}(\nu) \frac{-ig_W}{\sqrt{2}} \gamma_{\mu} P_L u(e^+) \right] \quad (\text{A.16})$$

where $P_L = (1 - \gamma^5)/2$ is the projector on left state helicity. Treating the W boson in the narrow width approximation means that, at the amplitude square level, the term coming from the W propagator is:

$$\frac{1}{(p_W^2 - M_W^2)^2 + M_W^2 \Gamma_W^2} \longrightarrow \frac{\pi}{M_W \Gamma_W} \delta(p_W^2 - M_W^2)$$

Therefore, we can replace the quantity in Eq. A.16 with an effective polarization:

$$\epsilon_W = \left(\frac{g_W^2}{2} \sqrt{\frac{\pi}{M_W \Gamma_W}} \right) \gamma^{\mu} P_L \left[\bar{u}_{-}(\nu) \gamma_{\mu} u_{-}(e^+) \right] \quad (\text{A.17})$$

at the amplitude level, while in the differential cross section:

$$d\Omega_W = \int \frac{d^3 p_{\nu}}{(2\pi)^3 2E_{\nu}} \frac{d^3 p_{e^+}}{(2\pi)^3 2E_{e^+}} \delta(p_W - p_{\nu} - p_{e^+}) \Big|_{p_W^2 = M_W^2} \quad (\text{A.18})$$

Appendix B

Amplitudes and cross sections formulas

In this section, we will present some formulas for amplitudes and cross sections.

B.1 Tree level amplitudes

For the tree level diagrams corresponding to the lowest order process in Figure 2-1, the amplitude can be written as :

$$\mathcal{M}_0 = \bar{u}(p_b) \not{\epsilon}_{W^+} \frac{\not{p}_t + m_t}{p_t^2 - \bar{m}_t^2} \Gamma_{\gamma, Z_0} \frac{-\not{p}_{\bar{t}} + m_t}{p_{\bar{t}}^2 - \bar{m}_t^2} \not{\epsilon}_{W^-} v(p_{\bar{b}}) \quad (\text{B.1})$$

with the following notations:

$$\begin{aligned} \Gamma_{\gamma, Z_0} = & [\bar{u}(p_2)(ie\gamma^\mu)u(p_1)] \frac{-i g_{\mu\nu}}{q^2} (-ieQ_t\gamma^\nu) + \\ & \left[\bar{u}(p_2) \left(-i \frac{g_W}{\cos \theta_W} \gamma^\mu \frac{1}{2} (V^e - A^e \gamma^5) \right) u(p_1) \right] \frac{-i g_{\mu\nu}}{q^2 - M_Z^2 + iM_Z\Gamma_Z} \times \\ & \left(-i \frac{g_W}{\cos \theta_W} \gamma^\nu \frac{1}{2} (V^t - A^t \gamma^5) \right) \end{aligned} \quad (\text{B.2})$$

(the first line represents the contribution of the photon exchange diagram, while the second line the contribution of the Z_0 boson exchange diagram). Here g_w is the weak coupling constant, θ_W is the Weinberg angle, and $Q_t = 2/3$ is the electric charge of the top quark in units of positive electron charge e . p_1 and p_2 are the momenta of the initial state electron and positron; $q^2 = (p_1 + p_2)^2$ is the square of the total energy available for the process. The couplings of the electron and top quark to the gauge boson Z_0 are given by the vector and axial coupling parameters:

$$\begin{aligned} V^e &= -\frac{1}{2} + 2 \sin^2 \theta_W, & A^e &= -\frac{1}{2} \\ V^t &= \frac{1}{2} - \frac{4}{3} \sin^2 \theta_W, & A^t &= \frac{1}{2} \end{aligned}$$

We shall usually denote by $\tilde{\mathcal{M}}$ the amplitudes multiplied by the denominators of the fermion propagators; for example:

$$\mathcal{M}_0 = \tilde{\mathcal{M}}_0 \frac{1}{p_t^2 - \bar{m}_t^2} \frac{1}{p_{\bar{t}}^2 - \bar{m}_t^2}$$

Throughout the paper, we also use the definitions:

$$p_t = p_{W^+} + p_b, \quad p_{\bar{t}} = p_{W^-} + p_{\bar{b}}, \quad \bar{m}_t^2 = m_t^2 - im_t \Gamma_t,$$

and k is the momentum of the gluon.

For the process with a real gluon radiated, the amplitudes are obtained by inserting the corresponding gluon polarization vector in the appropriate place, taking into account the extra fermionic propagator, and modifying the momenta in the appropriate way. For example, for the diagram with the gluon radiated from the top quark:

$$\mathcal{M}_t = \bar{u}(p_b) \not{\epsilon}_{W^+} \frac{\not{p}_t + m_t}{p_t^2 - \bar{m}_t^2} (-ig_s \not{\epsilon}_g) \frac{\not{p}_t + \not{k} + m_t}{(p_t + k)^2 - \bar{m}_t^2} \Gamma_{\gamma, Z_0} \frac{-\not{p}_{\bar{t}} + m_t}{p_{\bar{t}}^2 - \bar{m}_t^2} \not{\epsilon}_{W^-} v(p_{\bar{b}}) \quad (\text{B.3})$$

while for the diagram with the gluon radiated from the antibottom quark:

$$\mathcal{M}_{\bar{b}} = \bar{u}(p_b) \not{\epsilon}_{W^+} \frac{\not{p}_t + m_t}{p_t^2 - \bar{m}_t^2} \Gamma_{\gamma, Z_0} \frac{-\not{p}_{\bar{t}} - \not{k} + m_t}{(p_{\bar{t}} + k)^2 - \bar{m}_t^2} \not{\epsilon}_{W^-} \frac{-\not{p}_{\bar{b}} - \not{k} + m_b}{(p_{\bar{b}} + k)^2 - m_b^2} (-ig_s \not{\epsilon}_g) v(p_{\bar{b}}) \quad (\text{B.4})$$

Using the decomposition of the top propagator products described in section **3.1.1**, we obtain the following expressions for the gauge invariant amplitudes in Eq 3.6 :

$$\begin{aligned}
 \mathcal{M}_{prod} &= \left(\frac{\tilde{\mathcal{M}}_t}{2p_t k} + \frac{\tilde{\mathcal{M}}_{\bar{t}}}{2p_{\bar{t}} k} \right) \frac{1}{D(p_t)} \frac{1}{D(p_{\bar{t}})} \\
 \mathcal{M}_{tdecay} &= \left(-\frac{\tilde{\mathcal{M}}_t}{2p_t k} + \frac{\tilde{\mathcal{M}}_b}{2p_b k} \right) \frac{1}{D(p_t + k)} \frac{1}{D(p_{\bar{t}})} \\
 \mathcal{M}_{\bar{t}decay} &= \left(\frac{\tilde{\mathcal{M}}_{\bar{t}}}{2p_{\bar{t}} k} - \frac{\tilde{\mathcal{M}}_{\bar{b}}}{2p_{\bar{b}} k} \right) \frac{1}{D(p_t)} \frac{1}{D(p_{\bar{t}} + k)}
 \end{aligned} \tag{B.5}$$

where $D(p) = p^2 - \bar{m}_t^2$.

We also give here the amplitudes in the (extended) soft gluon approximation. The evaluation in this case proceeds as in Eqs. 3.8, 3.10, and we drop the $\not{\epsilon}_g \not{k}$ terms in the denominators of Eqs. 3.9, 3.11. Then

$$\tilde{\mathcal{M}}_{prod,tdecay}^{(t)}(ESGA) = (-ig_s) (2\epsilon_g p_t) \tilde{\mathcal{M}}_0 \tag{B.6}$$

and, evaluating the other amplitudes in a similar manner, we get:

$$\begin{aligned}
 \mathcal{M}_{prod}(ESGA) &= (-ig_s \epsilon_{g\mu}) \tilde{\mathcal{M}}_0 \left(\frac{p_t^\mu}{p_t k} - \frac{p_{\bar{t}}^\mu}{p_{\bar{t}} k} \right) \frac{1}{D(p_t)} \frac{1}{D(p_{\bar{t}})} \\
 \mathcal{M}_{tdecay}(ESGA) &= (-ig_s \epsilon_{g\mu}) \tilde{\mathcal{M}}_0 \left(-\frac{p_t^\mu}{p_t k} + \frac{p_b^\mu}{p_b k} \right) \frac{1}{D(p_t + k)} \frac{1}{D(p_{\bar{t}})} \\
 \mathcal{M}_{\bar{t}decay}(ESGA) &= (-ig_s \epsilon_{g\mu}) \tilde{\mathcal{M}}_0 \left(-\frac{p_{\bar{t}}^\mu}{p_{\bar{t}} k} + \frac{p_{\bar{b}}^\mu}{p_{\bar{b}} k} \right) \frac{1}{D(p_t)} \frac{1}{D(p_{\bar{t}} + k)}
 \end{aligned} \tag{B.7}$$

Neglecting the gluon momentum in the denominator of the propagators in the above equations (a valid approximation if the gluon energy is much smaller than the top width) we obtain the expression (Eq. 2.9) used in the evaluation of the infrared singular part of the cross section:

$$\mathcal{M}_{tot}^{sg} = (-ig_s \epsilon_{g\mu}) \mathcal{M}_0 \left(\frac{p_b^\mu}{kp_b} - \frac{p_{\bar{b}}^\mu}{kp_{\bar{b}}} \right) \tag{B.8}$$

B.2 Virtual corrections amplitudes

The amplitude for the general vertex correction in Figure 4-1 can be written as:

$$\delta\Gamma^\mu = \frac{\alpha_s}{4\pi} \int \frac{d^4k}{i\pi^2} \frac{1}{k^2} \gamma^\nu \frac{\not{p}_1 - \not{k} + m_1}{(p_1 - k)^2 - \bar{m}_1^2} \gamma^\mu (C_V + C_A \gamma^5) \frac{-\not{p}_2 - \not{k} + m_2}{(p_2 + k)^2 - \bar{m}_2^2} \gamma_\nu \quad (\text{B.9})$$

Upon evaluation of the integral, the result can be written in terms of two sets of form-factors; one for the vectorial part of the vertex correction, one for the axial part. The number of form factors needed depends on the specific constraints on the process; in our case, when the momenta p_1, p_2 are off-shell, we need eight \times 2 form factors:

$$\delta\Gamma_V^\mu = \frac{\alpha_s}{4\pi} \sum_{i=1,8} \left(C_V F_i^V T_i^{V\mu} + C_A F_i^A T_i^{A\mu} \right) \quad (\text{B.10})$$

The definition of these form factors depends on the choice of the spinorial elements in terms of which the result is written. In our case, we shall define:

$$\delta\Gamma_V^\mu = \frac{\alpha_s}{4\pi} C_V \times \quad (\text{B.11})$$

$$\begin{aligned} & \left[\begin{array}{cccc} p_1^\mu & F_1^V & + & \gamma^\mu & F_2^V + \\ (\not{p}_1 - m_1) p_1^\mu & F_3^V & + & (\not{p}_1 - m_1) \gamma^\mu & F_4^V + \\ p_1^\mu (-\not{p}_2 - m_2) & F_5^V & + & \gamma^\mu (-\not{p}_2 - m_2) & F_6^V + \\ (\not{p}_1 - m_1) p_1^\mu (-\not{p}_2 - m_2) & F_7^V & + & (\not{p}_1 - m_1) \gamma^\mu (-\not{p}_2 - m_2) & F_8^V \end{array} \right] \end{aligned}$$

for the vectorial part of the vertex correction; for the axial one, replace p_1^μ , γ^μ with $p_1^\mu \gamma^5$, $\gamma^\mu \gamma^5$ in the expression above. This definition has the advantage that when the particle i is on-shell, the terms which contain the $\pm \not{p}_i + m_i$ drop out. Also, we have made use of the fact that, if $\delta\Gamma^\mu$ multiplies A_μ in the full matrix element (A_μ can be thought of as the polarization vector of the weak gauge boson in diagram 4-1), then $(p_1 + p_2)^\mu A_\mu = 0$.

We shall evaluate and write the results for the form factors in terms of Passarino - Veltman functions (for the definition of these see section Appendix C):

$$F_1^V = 4[m_1(C_{12} - C_{11} + C_{23} - C_{21}) - m_2(C_{12} + C_{23})] \quad (\text{B.12})$$

$$F_2^V = -2[2p_1p_2(C_0 + C_{11}) + 2(C_{24} - 1/4) + 2B_0^{12} - 1 \\ - m_1m_2C_{11} + p_1^2(-C_{11} + C_{12}) - p_2^2C_{12}]$$

$$F_3^V = -4(C_0 + 2C_{11} - C_{12} + C_{21} - C_{23}) \quad , \quad F_4^V = 2m_2(C_0 + C_{11})$$

$$F_5^V = -4(C_0 + C_{11} + C_{23} + C_{12}) \quad , \quad F_6^V = 2m_1(C_0 + C_{11})$$

$$F_7^V = 0 \quad , \quad F_8^V = 2(C_0 + C_{11})$$

For the computation of the axial form factors, we can shift γ^5 in Eq. B.9 to the right, and then perform the same evaluations as in the vectorial case. In the result for the form factors, this amounts to changing the sign of m_2 , $m_2 \rightarrow -m_2$, and multiply the F_5, \dots, F_8 with (-1) . Then :

$$F_1^A = F_1^V + 8m_2(C_{12} + C_{23}) \quad , \quad F_2^A = F_2^V - 4m_1m_2C_{11} \quad (\text{B.13})$$

$$F_3^A = F_3^V \quad , \quad F_4^A = -F_4^V$$

$$F_5^A = -F_5^V \quad , \quad F_6^A = -F_6^V$$

$$F_7^A = -F_7^V \quad , \quad F_8^A = -F_8^V$$

The result 4.18 for the fermion self-energy corrections:

$$\Delta Z_2(p) = \left([\Sigma_a(p^2) + 2\Sigma_{ir}(p^2)] + \frac{\Sigma_{ir}(p^2)}{m}(\pm \not{p} - m) \right) \quad (\text{B.14})$$

can be similarly written in terms of Passarino-Veltman functions:

$$\Sigma_a(p^2) = \frac{\alpha_s}{4\pi}(1 + 2B_1(p^2, \bar{m}^2)) \quad (\text{B.15})$$

$$\Sigma_{ir}(p^2) = \frac{\alpha_s}{4\pi} \frac{m^2}{p^2 - \bar{m}^2} [4\Delta B_0(p^2, \bar{m}^2) + 4\Delta B_1(p^2, \bar{m}^2)]$$

with

$$\Delta B_n(p^2, \bar{m}^2) = B_n(p^2, \bar{m}^2) - B_n(\bar{m}^2, \bar{m}^2), \quad n = 0, 1$$

If we further define the X_0, X_1 form factors through:

$$\Delta Z_2(p) = 2 \frac{\alpha_s}{4\pi} [X_0(p^2) + X_1(p^2)(\pm \not{p} - m)] \quad (\text{B.16})$$

the renormalized vertex correction in Eq. 4.13:

$$\delta \Gamma_{ren}^\mu = \delta \Gamma^\mu + \frac{1}{2} \Delta Z_2(p_1) \Gamma^\mu + \frac{1}{2} \Gamma^\mu \Delta Z_2(p_2) \quad (\text{B.17})$$

can be obtained by making the following redefinitions of form-factors in Eq. B.12, B.13:

$$F_2^{V,A} \rightarrow F_2^{V,A} + X_0(p_1^2) + X_0(p_2^2) \quad (\text{B.18})$$

$$F_4^{V,A} \rightarrow F_4^{V,A} + X_1(p_1^2)$$

$$F_6^{V,A} \rightarrow F_6^{V,A} + X_1(p_2^2)$$

These general results are easily translated for the specific cases which appear in our computation. Take

$$F_{i,t\bar{t}}^{V,A} = F_i^{V,A}(p_1 = p_t, p_2 = p_{\bar{t}}, m_1 = m_2 = m_t)$$

for the correction to the top, antitop production vertex,

$$F_{i,tb}^{V,A} = F_i^{V,A}(p_1 = p_b, p_2 = -p_t, m_1 = m_b, m_2 = m_t)$$

for the correction to the top decay vertex, and

$$F_{i,\bar{t}b}^{V,A} = F_i^{V,A}(p_1 = -p_{\bar{t}}, p_2 = p_{\bar{b}}, m_1 = m_t, m_2 = m_b)$$

for the correction to the antitop decay vertex. Decomposing the top production and top decay interaction vertices in a vectorial and an axial part:

$$\Gamma_{\gamma, Z_0} = V^t \Gamma_{\gamma, Z_0}^{V, \mu} \gamma_\mu - A^t \Gamma_{\gamma, Z_0}^{A, \mu} \gamma_\mu \gamma^5 \quad (\text{B.19})$$

$$\not{\epsilon}_{W^+,W^-} = \frac{1}{2} \not{\epsilon}_{W^+,W^-}^{\mu} \gamma_{\mu} - \frac{1}{2} \not{\epsilon}_{W^+,W^-}^{A,\mu} \gamma_{\mu} \gamma^5$$

(see also Eqs. B.2, A.17) we can write:

$$\begin{aligned} \tilde{\mathcal{M}}_{t\bar{t}} &= \frac{\alpha_s}{4\pi} \sum_i \left[C_V^{t\bar{t}} F_{i,t\bar{t}}^V T_{i,t\bar{t}}^V + C_A^{t\bar{t}} F_{i,t\bar{t}}^A T_{i,t\bar{t}}^A \right] \\ \tilde{\mathcal{M}}_{tb} &= \frac{\alpha_s}{4\pi} \sum_i \left[C_V^{tb} F_{i,tb}^V T_{i,tb}^V + C_A^{tb} F_{i,tb}^A T_{i,tb}^A \right] \\ \tilde{\mathcal{M}}_{t\bar{b}} &= \frac{\alpha_s}{4\pi} \sum_i \left[C_V^{t\bar{b}} F_{i,t\bar{b}}^V T_{i,t\bar{b}}^V + C_A^{t\bar{b}} F_{i,t\bar{b}}^A T_{i,t\bar{b}}^A \right] \end{aligned} \quad (\text{B.20})$$

where

$$\begin{aligned} T_{i,t\bar{t}}^{(V,A)} &= \bar{u}(p_b) \not{\epsilon}_{W^+} (\not{p}_t + m_t) \Gamma_{\gamma,Z_0}^{(V,A),\mu} T_{i,t\bar{t},\mu}^{(V,A)} (-\not{p}_{\bar{t}} + m_t) \not{\epsilon}_{W^-} v(p_{\bar{b}}) \\ T_{i,tb}^{(V,A)} &= \bar{u}(p_b) \not{\epsilon}_{W^+}^{(V,A),\mu} T_{i,tb,\mu}^{(V,A)} (\not{p}_t + m_t) \Gamma_{\gamma,Z_0} (-\not{p}_{\bar{t}} + m_t) \not{\epsilon}_{W^-} v(p_{\bar{b}}) \\ T_{i,t\bar{b}}^{(V,A)} &= \bar{u}(p_b) \not{\epsilon}_{W^+} (\not{p}_t + m_t) \Gamma_{\gamma,Z_0} (-\not{p}_{\bar{t}} + m_t) \not{\epsilon}_{W^-}^{(V,A),\mu} T_{i,t\bar{b},\mu}^{(V,A)} v(p_{\bar{b}}) \end{aligned} \quad (\text{B.21})$$

and

$$C_V^{t\bar{t}} = V^t, \quad C_A^{t\bar{t}} = -A^t, \quad C_V^{tb} = C_V^{t\bar{b}} = \frac{1}{2}, \quad C_A^{tb} = C_A^{t\bar{b}} = -\frac{1}{2}.$$

B.3 Cross sections and color factors

The cross section for the generic process $(p_1 p_2) \rightarrow (p_i p_j \dots)$ can be written as:

$$d\sigma_{i \rightarrow f} = \frac{(2\pi)^4}{2E_1 2E_2 |v_1 - v_2|} \sum_{spins} |M_{i \rightarrow f}|^2 d\Omega_f \quad (\text{B.22})$$

where $d\Omega_f$ is the differential volume element in the final state phase space:

$$d\Omega_f = \prod_{final\,states} \frac{d^3 p_f}{(2\pi)^3 2E_f} \delta^4(P) \quad (\text{B.23})$$

The sum over spins in Eq. B.22 is performed over the spins of the final state particles. If we consider unpolarized electrons in the initial state, we sum over the helicities of these particles as well and multiply by a 1/4 average spin factor.

In the process under consideration here, the initial collision takes place in the center-of-mass frame. Therefore $E_1 = E_2 = W/2$, where W is the total available energy for the collision. Also, since the energies involved are much bigger than the electron mass (which is considered zero for all purposes in our computation), the speed of particles in the initial state is c .

Actually, in the formulas for the amplitudes presented in the previous sections there is an element missing. Since our final state particles include quarks and gluons, the amplitude for the process will contain a color index as well. However, because the experimental observables are colorless quantities, in the computation of the final cross section we have to sum over these color indices.

Since the initial state is colorless, the bottom and antibottom quarks in the final state of the lowest order process have the same color:

$$\mathcal{M}^0 \rightarrow \mathcal{M}_{ij}^0 = \mathcal{M}^0 \delta_{ij}$$

(here i would be the color index of the bottom quark, and j the color index of the antibottom quark). Summing over the colors in the cross section will give us a factor of 3:

$$\sigma^0 \sim \sum_{i,j} |\mathcal{M}_{ij}^0|^2 = 3 |\mathcal{M}^0|^2$$

In the case of a real gluon in the final state, taking the gluon coupling to a pair of quarks with color indices i, j to be $-ig_s T_{ij}^a$, we have:

$$\mathcal{M}^{rg} \rightarrow (\mathcal{M}^{rg})_{ij}^a = \mathcal{M}^{rg} T_{ij}^a$$

where a is the color index of the gluon. The matrices T_{ij}^a form a representation of the gauge group of QCD – SU(3). In order to perform the sum over the color indices, we use the relation:

$$Tr[T^a T^b] = \frac{1}{2} \delta_{a,b}$$

then:

$$\sigma^{rg} \sim \sum_{a,i,j} |\mathcal{M}^{rg}|^2 T_{ij}^a (T_{ij}^a)^* = \sum_a |\mathcal{M}^{rg}|^2 \text{Tr}[T^a T^a] = 4 |\mathcal{M}^{rg}|^2$$

The cross section in this case acquires a factor of 4 due to color summation.

In the case of virtual corrections, all the contributing amplitudes get a factor:

$$\mathcal{M}^{vg} \rightarrow (\mathcal{M}^{vg})_{ij} = (\mathcal{M}^{vg}) \sum_{a,k} T_{k,i}^a T_{k,j}^a = C_F \mathcal{M}^{vg} \delta_{ij}$$

Here k is the color index of the quarks inside the gluon loop. For the sum over color indices in the equation above, we have used:

$$\sum_a [T^a T^a]_{ij} = C_F \delta_{ij}, \quad C_F = \frac{N^2 - 1}{2N} = \frac{4}{3} \quad \text{for } N = 3$$

In the cross section, the virtual gluon contribution gets a factor of 3 from the sum over the color indices of the quarks in the final state. Note that the C_F factor is not included in the expressions for \mathcal{M}^{vg} throughout the paper.

Appendix C

Passarino-Veltman functions

The method of Passarino-Veltman (PV) functions [33] provides a systematic way of evaluating the tensor integrals appearing in the computation of loop corrections. For example, the result for the vertex correction integral B.9 can be written in terms of the following tensor functions:

$$\mathcal{C}^{\{0,\mu,\mu\nu\}} = \int \frac{d^4k}{i\pi^2} \frac{\{1, k^\mu, k^\mu k^\nu\}}{(k^2 - m_1^2) ((k + p_1)^2 - m_2^2) ((k + p_1 + p_2)^2 - m_3^2)} \quad (\text{C.1})$$

Following the Passarino-Veltman method, these functions can be written in term of scalar functions:

$$\begin{aligned} \mathcal{C}^\mu &= p_1^\mu \mathcal{C}_{11} + p_2^\mu \mathcal{C}_{12} \\ \mathcal{C}^{\mu\nu} &= p_1^\mu p_1^\nu \mathcal{C}_{21} + p_2^\mu p_2^\nu \mathcal{C}_{22} + (p_1^\mu p_2^\nu + p_2^\mu p_1^\nu) \mathcal{C}_{23} + g^{\mu\nu} \mathcal{C}_{24} \end{aligned} \quad (\text{C.2})$$

Furthermore, the \mathcal{C}_{ij} functions in the above equations can be written in terms of the scalar one-, two- and three-point integrals \mathcal{A}^0 , \mathcal{B}^0 and \mathcal{C}^0 . For completeness, we give here the formulas used to compute these functions (these formulas can be easily derived by multiplying the Eqs. C.2 by $p_{1\mu}$, $p_{2\mu}$, $g_{\mu\nu}$ and solving the resulting

systems of equations; they can also be found in [33]):

$$\begin{pmatrix} \mathcal{C}_{11} \\ \mathcal{C}_{12} \end{pmatrix} = X^{-1} \begin{pmatrix} \mathcal{B}_0^{(13)} - \mathcal{B}_0^{(23)} + f_1 \mathcal{C}^0 \\ \mathcal{B}_0^{(12)} - \mathcal{B}_0^{(13)} + f_2 \mathcal{C}^0 \end{pmatrix} \quad (\text{C.3})$$

$$\mathcal{C}_{24} = \frac{1}{4} + \frac{1}{4} \mathcal{B}_0^{(23)} + \frac{1}{2} m_1^2 \mathcal{C}^0 - \frac{1}{4} (f_1 \mathcal{C}_{11} + f_2 \mathcal{C}_{12}) \quad (\text{C.4})$$

$$\begin{pmatrix} \mathcal{C}_{21} \\ \mathcal{C}_{23} \end{pmatrix} = X^{-1} \begin{pmatrix} \mathcal{B}_1^{(13)} + \mathcal{B}_0^{(23)} + f_1 \mathcal{C}_{11} - 2\mathcal{C}_{24} \\ \mathcal{B}_1^{(12)} - \mathcal{B}_1^{(13)} + f_2 \mathcal{C}_{11} \end{pmatrix} \quad (\text{C.5})$$

$$\begin{pmatrix} \mathcal{C}_{23} \\ \mathcal{C}_{22} \end{pmatrix} = X^{-1} \begin{pmatrix} \mathcal{B}_1^{(13)} - \mathcal{B}_1^{(23)} + f_1 \mathcal{C}_{12} \\ -\mathcal{B}_1^{(13)} + f_2 \mathcal{C}_{12} - 2\mathcal{C}_{24} \end{pmatrix}.$$

Here we have used the following notations:

$$X = 2 \begin{pmatrix} p_1^2 & p_1 p_2 \\ p_1 p_2 & p_2^2 \end{pmatrix} \quad (\text{C.6})$$

$$f_1 = m_2^2 - m_1^2 - p_1^2 \quad (\text{C.7})$$

$$f_2 = m_3^2 - m_2^2 - (p_1 + p_2)^2 + p_1^2$$

$$\mathcal{B}^{\{0,\mu\}}(p_1, m_1, m_2) = \int \frac{d^4 k}{i\pi^2} \frac{\{1, k^\mu\}}{(k^2 - m_1^2)((k + p_1)^2 - m_2^2)} \quad (\text{C.8})$$

$$\mathcal{B}^\mu(p_1, m_1, m_2) = p_1^\mu \mathcal{B}_1(p_1^2, m_1^2, m_2^2)$$

$$2p_1^2 \mathcal{B}_1(p_1^2, m_1^2, m_2^2) = \mathcal{A}^0(m_1^2) - \mathcal{A}^0(m_2^2) + f_1 \mathcal{B}_0(p_1^2, m_1^2, m_2^2)$$

$$\mathcal{B}_n^{(12)} = \mathcal{B}_n(p_1^2, m_1^2, m_2^2) \quad (\text{C.9})$$

$$\mathcal{B}_n^{(13)} = \mathcal{B}_n((p_1 + p_2)^2, m_1^2, m_3^2)$$

$$\mathcal{B}_n^{(23)} = \mathcal{B}_n(p_2^2, m_2^2, m_3^2), \quad n = 0, 1$$

and, finally,

$$\mathcal{A}^0(m^2) = \int \frac{d^4 k}{i\pi^2} \frac{1}{(k^2 - m^2)}. \quad (\text{C.10})$$

The ultraviolet divergent integrals in the above expressions are evaluated with the help of the dimensional regularization method.

The above equations follow the standard definition of the PV functions; we shall denote the \mathcal{C} functions in Eq. C.1, C.2 by $\mathcal{C}^{\{\mu,\mu\nu\}}(p_1, p_2, m_1, m_2, m_3)$ and the \mathcal{C} functions in Eqs. C.3, C.5, C.5 by $\mathcal{C}_{ij}(p_1^2, p_2^2, m_1^2, m_2^2, m_3^2)$. The C function used in Appendix B are defined by:

$$C^{\{0,\mu,\mu\nu\}} = \int \frac{d^4k}{i\pi^2} \frac{\{1, k^\mu, k^\mu k^\nu\}}{(k^2 + i\epsilon) ((k - p_1)^2 - m_1^2) ((k + p_2)^2 - m_2^2)} \quad (\text{C.11})$$

$$C^\mu = -p_1^\mu C_{11} + (p_2 - p_1)^\mu C_{12} \quad (\text{C.12})$$

$$\begin{aligned} C^{\mu\nu} = & p_1^\mu p_1^\nu C_{21} + (p_2 - p_1)^\mu (p_2 - p_1)^\nu C_{22} - [p_1^\mu (p_2 - p_1)^\nu + (p_2 - p_1)^\mu p_1^\nu] C_{23} \\ & + g^{\mu\nu} C_{24} \end{aligned}$$

therefore:

$$C^{\{\mu,\mu\nu\}} = \mathcal{C}^{\{\mu,\mu\nu\}}(-p_1, p_2 - p_1, 0, m_1, m_2) \quad (\text{C.13})$$

$$C_0, C_{ij} = \mathcal{C}^0, \mathcal{C}_{ij}(p_1^2, (p_2 - p_1)^2, 0, m_1^2, m_2^2).$$

Moreover, the function B_0^{12} in Eq. B.12 is given by:

$$B_0^{12} = \mathcal{B}^0((p_1 + p_2)^2, m_1^2, m_2^2) \quad (\text{C.14})$$

and in Eqs. B.15:

$$B_n(p^2, m^2) = \mathcal{B}_n(p^2, 0, m^2), \text{ for } n = 0, 1. \quad (\text{C.15})$$